An 11-year Global Gridded Aerosol Optical Thickness Reanalysis (v1.0) for Atmospheric and Climate Sciences

Peng Lynch[1], Jeffrey S. Reid[2], Douglas L. Westphal[2], Jianglong Zhang[3], Timothy F. Hogan[2], Edward J. Hyer[2], Cynthia A. Curtis[2], Dean A. Hegg[4], Yingxi Shi[3], James R. Campbell[2], Juli I. Rubin[5], Walter R. Sessions[1,6], F. Joseph Turk[7], and Annette L. Walker[2]

1. Computer Sciences Corporation Inc., Monterey, CA, USA
2. Marine Meteorology Division, Naval Research Laboratory, Monterey, CA, USA
3. Dept. of Atmospheric Science, University of North Dakota, Grand Forks, ND, USA
4. Dept. of Atmospheric Science, University of Washington, Seattle, WA, USA
5. National Research Council Postdoctoral Research Associate, Monterey, CA, USA
6. Dept. of Atmospheric and Oceanic Sciences, University of Wisconsin-Madison, WI, USA
7. Jet Propulsion Laboratory, Pasadena, CA, USA

Correspondence to: Peng Lynch, CSC Inc., Mail: Marine Meteorology Division, Naval Research Laboratory, 7 Grace Hopper Ave, Stop 2, Monterey, CA 93943. Email: peng.lynch.ctr@nrlmry.navy.mil

Abstract

While standalone satellite and model aerosol products see wide utilization, there is a significant need in numerous atmospheric and climate applications for a fused product on a regular grid. Aerosol data assimilation is an operational reality at numerous centers, and like meteorological reanalyses, aerosol reanalyses will see significant use in the near future. Here we present a

standardized 2003 - 2013 global 1x1 degree and 6-hourly modal aerosol optical thickness (AOT) reanalysis product. This dataset can be applied to basic and applied earth system science studies of significant aerosol events, aerosol impacts on numerical weather prediction, and electro-optical propagation and sensor performance, among other uses. This paper describes the science of how to develop and score an aerosol reanalysis product. This reanalysis utilizes a modified Navy Aerosol Analysis and Prediction System (NAAPS) at its core and assimilates quality controlled retrievals of AOT from the Moderate Resolution Imaging Spectroradiometer (MODIS) on Terra and Aqua and the Multi-angle Imaging SpectroRadiometer (MISR) on Terra. The aerosol source functions, including dust and smoke, were regionally tuned to obtain the best match between the model fine and coarse mode AOTs and the Aerosol Robotic Network (AERONET) AOTs. Other model processes, including deposition, were tuned to minimize the AOT difference between the model and satellite AOT. Aerosol wet deposition in the tropics is driven with satellite retrieved precipitation, rather than the model field. The final reanalyzed fine and coarse mode AOT at 550 nm is shown to have good agreement with AERONET observations, with global mean root mean square error around 0.1 for both fine and coarse mode AOTs. This paper includes a discussion of issues particular to aerosol reanalyses that make them distinct from standard meteorological reanalyses, considerations for extending such a reanalysis outside of the NASA A-Train era, and examples of how the aerosol reanalysis can be applied or fused with other model or remote sensing products. Finally, the reanalysis is evaluated in comparison with other available studies of aerosol trends, and the implications of this comparison are discussed.

1.0 Introduction

The importance of aerosol particles in the atmosphere and climate system is recognized across the earth sciences. Long implicated in climate change investigations (e.g., IPCC 2007; 2013), aerosol particles influence countless other aspects of science and society. Obvious impacts include biologic and visual air quality, including health outcomes (Laden et al., 2000; Kappos, et al., 2004), defense operations, and transportation (Wilkinson et al., 2012). Further, aerosol particles interfere with many aspects of earth system surveillance, such retrievals of sea surface temperature (e.g., May et al., 1992; Reynolds, 1989; Robock, 1989) and ocean color (e.g., Gordon, 1997) and land use systems (Song et al., 2001). Aerosols can also affect atmospheric retrievals or radiances used to constrain temperature, water vapor, and CO_2 in numerical weather prediction models (Houweling et al., 2005). In all of the above cases, contiguous spatial and temporal sampling of aerosol loadings is critical. Monitoring solutions using satellite data alone must cope with variable orbits (polar, high inclination or geostationary) and sampling times. Based on this large basic applied science need, there is considerable demand for consistent gridded aerosol products constructed for numerous applications.

To meet aerosol monitoring requirements, the climate and earth systems science community has historically presented aerosol data as either a free-running model (with the advantage of regularly gridded and timed products, e.g., Tanaka et al., 2003; Miller et al.,2006; Morcrette et al., 2009; Colarco et al., 2010; Pérez et al., 2011), or irregularly-timed and located satellite data (e.g., Mishchenko et al., 1999; Torres et al., 2002; Hsu et al., 2004; Levy et al., 2010; Kahn et al., 2010). In both cases, the products are underdetermined. Models have poorly-resolved emissions, evolution, and sinks, and can be affected by errors in the underlying meteorological model, whereas satellite data has limited coverage and underdetermined retrievals based on assumptions that lead to a series of spatially and temporally-correlated biases (e.g., Shi et al., 2011a). Ultimately, models and remote sensing products present

68 different aspects of atmospheric characteristics. When model and satellite products are compared,
69 contextual and sampling biases appear (e.g., Zhang and Reid, 2009). For daily and more rapid analysis,
70 such as for many specific earth system science process study questions or intersensor correction,
71 neither approach can adequately represent the full state of the aerosol system.

72 To bridge modeling and remote sensing data sources, numerous operational numerical weather
73 prediction centers have embarked on sophisticated aerosol data assimilation efforts of both passive and
74 lidar satellite sensors (e.g, Collins et al., 2001; Weaver et al., 2007; Zhang et al., 2008, 2011; Benedetti et
75 al., 2009; Sekiyama et al., 2010). Satellite products are screened, empirically corrected and assimilated
76 into models to provide systematic best-available analyses of the aerosol environment. The next step in
77 this process is to develop best-available reanalyses for community use. Just as meteorological reanalysis
78 such as the NCAR/NCEP (eg., Kalnay et al., 1996) and ECMWF (eg., Uppala et al., 2005; Dee et al., 2011)
79 are commonly applied for meteorological applications, aerosol reanalyses are likely to be destined to be
80 useful data sources for initial analysis or systematic global studies for aerosol sciences.

81 Like meteorological reanalyses, aerosol reanalyses are generated through a rerun of a model that
82 assimilates historical observational data. Aerosol reanalyses aim to be a best-available, contiguous,
83 gridded product with consistent temporal reporting. It combines advantages of data accuracy from
84 satellite products and data consistency from modelling. The data should have good spatial and temporal
85 coverage and be easy to use. But an aerosol reanalysis is not simply just a rerunning of the model with
86 aerosol data assimilation. First, strict quality assurance and quality control processes need to be applied
87 to the satellite data that goes into an assimilation system, such that the model input is as consistent as
88 possible over the reanalysis period. Biased retrievals in the data assimilation system could result in
89 erroneous features that can propagate in the short term. Lack of consistency in the model or data can
90 lead to artifacts that could be mistaken for climatological trends or spurious aerosol events. Second,

91 the performance of the underlying aerosol forward model should be optimized to its upper limit through
92 a series of tunings to the aerosol sources and wet/dry removal processes. This helps to avoid large and
93 frequent corrections via the data assimilation cycle, so that the natural model field is as close as possible
94 to the satellite product and the final reanalysis product is smooth and fluent in space and time.

95 In this paper, we present the Naval Research Laboratory's development of an aerosol reanalysis
96 product for applied science use through the assimilation of NASA Terra and A-train satellite sensors into
97 the Navy Aerosol Analysis and Prediction System (NAAPS). The goal is to provide a best available AOT
98 product for applications that require this parameter. As the system develops and verification datasets
99 become available, the publically-released analysis will include many other aspects of the aerosol system,
100 including three dimensional concentrations and radiative effects such as fluxes and heating rates. Our
101 goals for the initial development of the NAAPS reanalysis and this paper are threefold.

102 a) *Development of a baseline applications dataset:* NAAPS has always been operationally focused,
103 with frequent operational transitions. In support of basic research and climatology applications,
104 however, the NAAPS model often requires re-runs with updated parameterizations. With
105 individual case studies being examined dozens of times per year, we wish to support such
106 endeavors by developing an accurate AOT product that is consistent in quality and time.
107 b) *Development of a baseline verification dataset:* Any application of the baseline dataset will
108 require a comprehensive description of the NAAPS model when run in reanalysis mode, and
109 how this differs from the operational version of NAAPS. The methods and data for characterizing
110 the reanalysis performance must be carefully examined and documented.
111 c) *Development of a framework for future development:* We wish to investigate the degree a
112 reanalysis represents the true atmospheric state and the extent that it can be used to study
113 climatologically-relevant aerosol features like trend and radiative impacts. As more satellite

products mature, they can also be incorporated into the reanalysis. The analysis presented here is intended to be a template for characterization of future reanalysis datasets as they become available.

While the aerosol system is a highly complex internal mixture of anthropogenic, biogenic, open burning and wind driven emissions, ultimately it is AOT and its simple partition into fine and coarse mode contributions that we can actually measure and verify globally. Reanalyses on atmospheric gas composition and/or aerosols are also in development at ECMWF (Inness et al., 2013) and NASA (Buchard et al., 2015). The aerosol models used for generating these reanalyses are independent in their underlying meteorology, as well as aerosol sources, sinks, microphysics and chemistry. The AOT assimilation methodologies, the observed AOT data to be assimilated, and the pre-assimilation treatments of input data are also different. Validation of multivariate reanalyses of atmospheric composition is a very complex task, and a comprehensive evaluation is needed. This study focuses exclusively on the development and validation of a 550 nm modal (fine mode, coarse mode and total) AOT reanalysis.

In this paper, we provide an up-to-date description of the primary NAAPS model, noting differences between the reanalysis and operational versions. Our emphasis is on the development of a modal NAAPS AOT analysis. We describe the methods used to tune modeled aerosol processes. The data assimilation system used to fuse the model and observations is described, as well as the satellite data products used in the reanalysis. This is followed by a basic description of the reanalyzed global fine and coarse mode 550 nm AOT fields and their verification. We conclude with a brief synopsis and discussion of our findings. We provide documentation of strengths and pitfalls of reanalysis products including advice on interpreting like products. For example, we discuss how the data assimilation system affects diurnal aerosol representation or how long term trends are represented in the simulation that has static

137 industrial emissions. We also discuss the difficulty in keeping meteorological input consistent at decadal
138 levels. We conclude with a project synopsis and outlook for future experiments.

139

140 **2.0 Description of Model: NAAPS and NAVDAS-AOT**

141 The foundation of this AOT reanalysis is the Navy Aerosol Analysis and Prediction System (NAAPS)
142 and its associated aerosol data assimilation components. NAAPS is an offline aerosol transport model,
143 which has seen wide use in the community for global aerosol lifecycle research, contextual information,
144 field mission planning, and operations.

145 The original NAAPS model was based on the Danish Eulerian Hemispheric Model (Christensen,
146 1997), although since then there have been a number of upgrades to model advection and microphysics.
147 NAAPS has been run quasi-operationally at NRL since 1998, and became the world's first operational
148 global aerosol model in 2006 with implementation at the Fleet Numerical Meteorology and
149 Oceanography Center (FNMOC). The Navy Atmospheric Variational Data Assimilation System (NAVDAS)
150 for Aerosol Optical Thickness (NAVDAS-AOT; Zhang et al., 2008) was operationally implemented in 2010.
151 The system assimilates quality assured and quality controlled 2-dimensional MODIS AOT at 550 nm. In
152 its current operational configuration, NAAPS makes 6-day forecasts, 4 times a day at 1080x540 global
153 (1/3 degree) spatial resolution and 42 vertical levels driven by truncated T425L60 resolution Navy Global
154 Environmental Model (NAVGEM) meteorology (Hogan et al., 2014). Papers describing the development
155 of the operational NAAPS include Witek et al. (2007) for sea salt, Reid et al. (2009) for biomass burning
156 smoke and Westphal et al. (2009) for dust. Updates to the operational model can be found at
157 http://www.nrlmry.navy.mil/aerosol/.

158 In converting NAAPS from a forecast model to a reanalysis system for the A-train 2003-2013
159 time period, we desire a system that is consistent spatially and temporally in time and fits within our
160 computational constraints. This requires, at times, significant departures from the operational model,

and some reduction in resolution. In this section, we describe the NAAPS model configured for reanalysis mode, its AOT assimilation package and the associated MODIS, MISR and precipitation satellite data used to initialize and assimilate into the model. We also describe the tuning processes necessary to help ensure spatial and temporal consistency within the reanalysis period.

2.1 Meteorology fields

The current operational version of NAAPS is driven by NAVGEM (Hogan et al., 2014), a global T425L60 spectral model that is only available since September 2013. The NAAPS reanalysis described in this paper is driven by the recently-decommissioned Navy Operational Global Atmospheric Prediction System (NOGAPS) analysis fields for 2003-2013. A full NAVGEM reanalysis is under construction that will allow higher horizontal and vertical resolution to better constrain future runs of the reanalysis. The NOGAPS model is a global model that is spectral horizontally and energy-conserving finite-difference (sigma coordinate) in the vertical (Hogan and Rosmond, 1991; Hogan and Brody, 1993). Four times a day, the weather forecast models provide 6-day forecasts of the dynamical and surface analysis fields to NAAPS at 3-hr intervals. The reanalysis uses only the 00, 06, 12, and 18Z analyses with the associated 3-hr forecast fields to make up the 3-hr time series of dynamical forcing. NOGAPS variables used by NAAPS are the topography, sea ice, surface stress, surface heat flux, surface moisture flux, surface temperature, surface wetness, snow cover, stratiform precipitation, convective precipitation, lifting condensation level, cumulus fractional coverage, cumulus cloud height, surface pressure, three components of the wind, temperature, and relative humidity. For data assimilation, NOGAPS uses the NRL Atmospheric Variational Data Assimilation System (NAVDAS), which is still used operationally for assimilation of a large variety of conventional and satellite-based observations (Daley et al., 2001). While NOGAPS has had some resolution changes over the 2003-2013 study period (ranging from T159 to T319),

183 spectrally truncated NOGAPS meteorology data is incorporated into the NAAPS reanalysis for each 6
184 hour time step at the prescribed 1x1 degree resolution.

185 As the primary sink of aerosol particles, the precipitation component of NOGAPS is worth special
186 attention. Often in large scale models the parametrized precipitation schemes for tropical regimes
187 generate widespread light precipitation, while the long-term total precipitation amount is comparable
188 to observations (Dai, 2006, Sun et al., 2007). Similarly, global models also have difficulty placing
189 significant convective cells, particularly moderately-sized squall lines or coastal thunderstorms. Diurnal
190 precipitation cycles are also poorly represented by numerical models. These characteristics of model
191 precipitation are shown to affect removal of aerosol particles and can have significant impact on
192 regional AOT simulations (Wilcox and Ramanathan, 2004; Xian et al., 2009). For the reanalysis, tropical
193 precipitation from NOAA Climate Prediction Center (CPC) MORPHing technique (CMORPH, Joyce et al.,
194 2004) is used whenever available to improve aerosol wet deposition in the manner described in Xian et
195 al. (2009), in which cloud structure from the model is retained but precipitation flux is changed
196 accordingly. CMORPH combines infrared (IR) and passive microwave data (PMW) retrieved from
197 instruments onboard multiple geostationary and lower-orbiter satellites. CMORPH was chosen for this
198 role as it appears to have the best representation of temporal and spatial patterns of tropical
199 precipitation among satellite precipitation products (Janowiak et. al, 2005; Sapiano and Arkin, 2009).
200

201 2.2 Aerosol Model

202 As noted above, NAAPS is a global aerosol model originated in the mid-1990's from a
203 hemispheric sulfate chemistry model developed by Christensen (1997). Dust, sea salt and smoke have
204 been added to the original model, and are documented in Westphal et al. (2009), Witek et al. (2007) and
205 Reid et al. (2009), respectively. Given that what is commonly referred to as regional pollution or haze is

a result of complex anthropogenic and biogenic emissions and chemistry, here we replaced the simplified Christensen (1997) SO_2 and sulfate chemistry. As elaborated in Section 2.2.6, anthropogenic SO_2, sulfate and organics, are combined with biogenic emissions to form an anthropogenic and biogenic fine (ABF) aerosol particle species.

2.2.1 Aerosol Model Dynamics

The equations solved in the model have the form

$$\frac{\partial q_i}{\partial t} = -\left(u\frac{\partial q_i}{\partial x} + v\frac{\partial q_i}{\partial y} + \dot{\sigma}\frac{\partial q_i}{\partial \sigma}\right) + \left(K_x\frac{\partial^2 q_i}{\partial x^2} + K_y\frac{\partial^2 q_i}{\partial y^2} + \frac{\partial(\Gamma^2 K_z\frac{\partial q_i}{\partial \sigma})}{\partial \sigma}\right) + P_i - Q_i \quad , \qquad (1)$$

where q_i is the mass mixing ratio (kg kg^{-1}) for the species *i*, $q_i = c_i/\rho$, where c_i is the mass concentration (kg m^{-3}) and ρ is the density of air (kg m^{-3}), *x* and *y* are the horizontal coordinates (in meter along longitude and latitude directions), σ is the terrain-following vertical coordinate ($\sigma = p/p_s$, where *p* is the present pressure and p_s surface pressure) that ranges from 1 at the surface to 0 at the model top, $u, v, \dot{\sigma}$ are the advection velocity in the *x, y* and the vertical directions of the σ-coordinates, K_x and K_y are horizontal diffusion coefficients that are assumed to be constant ($K_x = K_y = 6\times10^4$ m^2 s^{-1}), And K_z is the vertical diffusion coefficient based on the Monin-Obukhov similarity theory for the surface layer (Obukhov, 1971). The K_z profile is extended to the whole boundary layer by using a simple extrapolation (Hertel et al., 1995). Finally, $\Gamma = d\sigma/dz$ (m^{-1}). P_i are the sources and Q_i are the sinks for the species *i*.

Equation 1 is solved on a spherical grid with 1° x 1° horizontal resolution and 25 vertical irregular σ-coordinate levels in the reanalysis product presented here. The average depth of the first layer is ~30 meters, and consecutive layers gradually increase in depth towards the top layer, which ends at ~18 km (70hpa). Advection is calculated using a semi-Lagrangian scheme (Staniforth and Cote, 1991), with departure points calculated using the method of Ritchie (1987). Horizontal and vertical diffusion are calculated with a finite-element method (e.g., Bathe, 2006).

228 2.2.2 Aerosol Optical Properties in NAAPS

229 Aerosol microphysics are treated relatively simply in NAAPS. This is in response to the
230 computational needs of an efficient operational forecast model, its operational requirements (e.g.,
231 forecast severe visibility reducing events) and the fact that in comparison with the uncertainties in
232 source functions as well as transport meteorology, microphysics is relatively well constrained. Dry mass
233 concentrations are forecasted with Equation 1 and AOT for each aerosol species is computed assuming
234 an effective particle size with respect to mass. Aerosol particles in NAAPS are treated as external
235 mixture of the aforementioned species and do not interact with each other. With these assumptions,
236 extinction and AOT can be calculated using bulk values of optical properties that have been derived from
237 theory and observations. The calculations for scattering (b_{scat}, m^{-1}), absorption (b_{abs}, m^{-1}) and extinction
238 coefficients (b_{ext}, m^{-1}), plus the integrated optical thickness (τ, unitless) are, respectively

239 $$b_{scat,i}(\lambda, x, y, \sigma) = c_i(x, y, \sigma)\alpha_{scat,i}(\lambda)\, f_i[r(x, y, \sigma)]) \quad , \quad (2)$$

240 $$b_{abs,i}(\lambda, x, y, \sigma) = c_i(x, y, z)\alpha_{abs,i}(\lambda) \quad , \quad (3)$$

241 $$b_{ext,i}(\lambda, x, y, \sigma) = b_{scat,i}(\lambda, x, y, \sigma) + b_{abs,i}(\lambda, x, y, \sigma) \quad \text{, and} \quad (4)$$

242 $$\tau_i(\lambda, x, y) = \int_1^0 b_{ext,i}(\lambda, x, y, \sigma)\, \frac{1}{\Gamma} d\sigma \quad , \quad (5)$$

243 where α_{ext}, α_{scat}, *and* α_{abs} are the mass extinction, scattering, and absorption efficiencies respectively
244 ($m^2\, g^{-1}$), and f_i is a scattering hygroscopic growth factor.

245 The bulk mass extinction, scattering, and absorption efficiencies, along with single scattering
246 albedo and asymmetry factor for the four aerosol species at wavelength λ = 550 nm are given in Table 1.
247 For ABF, dust and sea salt, the values are taken from the optical properties of aerosol and clouds-OPAC
248 database (Hess et al., 1994). The chosen coefficients for ABF are weighted towards the more-absorbing
249 aerosol particles that are generated by less-developed countries that dominate global aerosol fields

(Dubovik et al., 2002). Optical properties for smoke are treated similarly, with both empirical derivations and theory derived from Reid et al. (2005a, b).

The effect of humidity on particle light scattering for each aerosol species is represented by the Hänel (1976) formulation of the hygroscopic growth factor $f_i(r)$ (unitless), defined as

$$f_i(r) = \left[\frac{(1-r)}{(1-r_o)}\right]^{-\gamma_i}, \quad (6)$$

where r is the relative humidity, γ_i is an empirical species-dependent exponent and r_o is the reference relative humidity that is set equal to 30%. In NAAPS, γ_i is taken as 0.5 for ABF particles assuming 40% sulfate and 60% organic aerosols. In comparison, γ_i is 0.63 for sulfate (Hänel, 1976), 0.18 for smoke (Reid et al., 2005b), 0.46 for sea salt (Hegg et al. 2002; Ming and Russell, 2001), and zero for dust (Li-Jones et al., 2002). A maximum allowed r is 95%. We assume absorption α_{abs} is not affected by humidity.

2.2.3 Sink processes in NAAPS

Dry deposition to the surface is accounted for through a decrease of the aerosol concentration in the lowermost model layer, assuming a dry deposition flux

$$F_{DDi} = c_{1i} v_{di} \quad , \quad (7)$$

where c_{1i} is the mass concentration (kg m^{-3}) in the first layer above the surface for the species i, and v_{di} is the dry deposition velocity, which is a function of aerosol type and surface type.

For particle deposition over water, the dry deposition velocity v_d is set to 0.0002 m s^{-1} for anthropogenic and biogenic fine particles, 0.0003 m s^{-1} for smoke loosely following the theoretical relation between over water v_d and particle radius in Slinn and Slinn (1980), assuming bulk effective radius listed in Table 1 for the two types of aerosols. v_d is set to 0.001 m s^{-1} over water for dust particles after tuning to minimize AOT corrections through the data assimilation process (more details in section

2.4.2). Dry deposition of sea salt to open water is given by the formula in Slinn and Slinn (1980), assuming a dry mass mean radius near 1.5 μm, and written as

$$v_{dss} = C_d U_{10}, \tag{8}$$

where $C_d = 1.3 \times 10^{-3}$ is the drag coefficient, and U_{10} the wind speed at 10 meters above the sea surface in m s^{-1}.

For particle deposition over land, the method of Walcek et al. (1986) is used and the explicit expression for v_d is the same as in Christensen (1997; Eq. (9)), which is a function of surface friction velocity and Monin-Obukhov length, which is a measure of the stability of the surface layer (Obukhov, 1971, Eq. 26). This is written as

$$v_d = \begin{cases} \dfrac{u_*}{a}\left(1+\left(\dfrac{-300}{L}\right)^{2/3}\right) & for\ L<0 \\ \dfrac{u_*}{a} & for\ L>0 \end{cases}, \tag{9}$$

where u_* is the surface friction velocity in m s^{-1}, a = 500 (except for a forest with leaves, where a = 100), and L is the Monin-Obukhov length. v_d is calculated using Eq. (9) for all the aerosol species in the model.

Gravitational settling is also applied to the aerosol particles in the model. Dry deposition is only applied in the lowermost model layer, whereas gravitational sedimentation takes place within the whole vertical domain except the lowermost model layer, as it is taken into account in v_d.

The wet deposition of particles is assumed to be similar to that for sulfate aerosol, based on a simple scavenging ratio formulation (e.g. Iversen, 1989). The scavenging coefficient is calculated in the same way as in Witek et al. (2007), as a function of the precipitation mass flux with different below-cloud and in-cloud scavenging ratios, written as

288 $$W(\sigma) = \begin{cases} \dfrac{\Lambda_{bc}}{H}\dfrac{P_a(\sigma)}{\rho_w} & \text{below cloud scavenging} \\ \dfrac{\Lambda_c}{H}\dfrac{P(\sigma)}{\rho_w} & \text{in cloud scavenging} \end{cases} , \quad (10)$$

289 where $P_a(\sigma)$ and $P(\sigma)$ (kg m^{-2}s^{-1}) are the total downward flux densities of precipitation mass at a
290 given σ-level below or in a precipitating cloud, respectively. H is an effective thickness for scavenging
291 (set to 1000 m), Λ_{bc} = 1×10^5 is the below-cloud scavenging ratio, Λ_c = 7×10^5 is the in-cloud
292 scavenging ratio, and ρ_w is the density of water.

293 2.2.4 Dust

294 Dust emissions occur whenever the friction velocity exceeds a threshold value, snow depth is
295 less than a critical value, and the surface moisture is less than a critical value (Westphal et al., 1988).
296 The dust emission flux follows the equation

297 $$F_{dust} = c\, e_f u_*^4 , \quad (11)$$

298 where e_f is the erodible fraction of a grid box (unitless), u_* is the surface friction velocity with the
299 threshold value of 0.6 m s^{-1} for dust mobility, and c is a scaling constant of 4.5 x10^{-7} g m^{-2} s^{-1}. In the
300 operational version of NAAPS, the erodibility map is empirically derived from the United States
301 Geological Survey Land Cover Characteristic Database and Total Ozone Mapping Spectrometer Aerosol
302 Index values (Walker et al., 2009). While in general the operational version of NAAPS has good dust
303 scores, NAAPS clearly has a high bias for dust for the Sahara. For the reanalysis, the use of Ginoux et al.
304 (2001) dust sources mitigated much of this bias. The Ginoux et al. (2001) erodibility map associates dust
305 sources with topographic depressions and has many of the same features as seen in Westphal et al.
306 (1988), yet its geologic input data tightened individual source areas.

307 Regional source tuning is also applied in the NAAPS reanalysis, which is described in Section 2.4.
308 Dust is emitted into the bottom two layers of the model (below 100m) when friction velocity exceeds
309 the threshold and surface wetness is below a critical value (0.4). Then, dust is transported by model

dynamics both horizontally and vertically in the boundary layer and the free troposphere. Dust removal includes sedimentation, dry deposition and wet removal, which is constrained with CMORPH precipitation within the tropics. Dust is assumed to be totally hydrophobic and hence the hygroscopic growth factor is set to 1.

2.2.5 Sea Salt

The sea salt component for operational NAAPS and the NAAPS reanalysis was developed by Witek et al. (2007). Sea salt emissions are driven dynamically by sea surface wind. The sea salt dry mass flux F_{ssa} (kg $m^{-2}s^{-1}$) from the surface is based on the whitecap method and the Monahan's formulation of the source function (Monahan et al., 1986), and has the empirical form

$$F_{ssa} = a_s U_{10}^{b_s} \quad , (12)$$

where U_{10} is the wind speed at 10 meters above the sea surface in m s^{-1}, $a_s = 1.37 \times 10^{-13}$ and $b_s = 3.41$ for particles with diameters from 1.6 to 16 µm. Dry deposition of sea salt over water is proportional to the sea surface wind speed, following Slinn and Slinn (1980) and over land follows Eq. (9). Sea salt particles are assumed to undergo hygroscopic growth depending on ambient atmospheric relative humidity, following the growth rate shown in Eq. (6). Sea salt scattering coefficient is based on swelled particles, while absorption coefficient is assumed not effected by the swell.

2.2.6 Anthropogenic and biogenic fine particles (ABF)

The most significant change to NAAPS microphysics for the reanalysis is the development of a method to account for complex anthropogenic and biogenic species while not significantly increasing the computational cost of the model. Originally, the only anthropogenic emissions and predictive variables within NAAPS were SO_2 and sulfate. However, organic species constitute one of the most important contributors to the mass of atmospheric aerosols (Zhang et al., 2007, Jimenez et al., 2009), and indeed commonly dominate the submicron aerosol mass and AOT. This organic aerosol mass, while having a significant component attributable to primary organic aerosol (POA) emission, is predominantly

secondary organic aerosol (SOA; i.e., created in the atmosphere from volatile organic carbon (VOC) precursors in the gas phase, such as, isoprene, terpenes and aromatics; e.g., Zhang et al, 2007). These precursors are largely biogenic in origin. Ultimately, the complex chemical interactions between anthropogenic and biogenic emissions result in a photochemical soup that cannot be directly linked to a single origin.

For realistic simulation of AOT, primary and secondary organic aerosols must both be included in the NAAPS model in some form. To be consistent with the NAAPS reanalysis' philosophy of simple and tractable physics, the sulfur-related species has been replaced with a bulk anthropogenic and biogenic fine (ABF) mass category to account for the entire class of anthropogenic and biogenic emissions and their secondary particle products. This species class includes all accumulation mode particles, including biogenic marine, outside of open biomass burning, as described in Section 2.2.7. The first component of this mixture is the original sulfur chemistry. Sulfate aerosols are produced by chemical processes in the atmosphere from gaseous precursors, mainly sulfur dioxide (SO_2) from anthropogenic sources and dimethylsulfide (DMS) from biogenic sources. For NAAPS reanalysis, SO_2 emissions are updated from GEIA Version 1A (i.e., 1985) (Benkovitz, 1996) to Monitoring Atmospheric Composition & Climate/CityZen EU projects (MACCity) inventory 2005-2010 average (Granier et al., 2011, Diehl et al., 2012), which reflects the increased emission in India and China over the past decade and also includes monthly variation. DMS emission fluxes at the air-sea interface are computed using the Saltzman (1993) parameterization, with the monthly DMS seawater concentrations from Lana et al. (2011). DMS are immediately converted to 95% sulfur dioxide and 5% sulfate in the model. SO_2 chemistry follows Hoffmann and Calvert (1985), in which oxidation of sulfur solution (S(IV)) by hydrogen peroxide (H_2O_2) and dissolved ozone (O_3) are considered climatologically. We assume background oxidants H_2O_2 and O_3 are not depleted by reactions. Ultimately, sulfur chemistry accounts for roughly one half of all non-biomass burning fine mode AOT.

Inclusion of POA in the NAAPS reanalysis is straightforward, including the major VOC species that act as precursors for the SOA. We apply the 2005-2010 monthly-mean MACCity data base for anthropogenic (industrial and transport) emissions of POA and SOA precursors (Granier et al., 2011), the Bond et al (2004) biofuels data with a monthly scaling factor based on Jeong (2011), and the Precursors of Ozone and their Effects in the Troposphere (POET) climatological monthly emissions inventory for biogenic VOC's (Olivier et al., 2003). For the actual SOA formation process, the Volatility Basis Set (VBS) approach has been adopted (Donahue et al., 2006; Ahmadov et al., 2012). This greatly reduces both the number of necessary precursor species and the number of SOA products from the vast numbers needed to explicit represent SOA formation and evolution by formulating the conversion process in terms of a limited number of precursor species and volatility classes (four in our case) for the reaction products. The reaction yields for the various VBS classes, upon which the approach ultimately depends, are derived from numerous chamber studies as cited, for example, in Ahmadov et al. (2012) and Donahue et al. (2006). Phase partitioning is done as per Pankow (1994).

To further simplify the inclusion of organic aerosols in the NAAPS model, both the POA and SOA are calculated in a "preprocessor" at model initialization. For the SOA, this includes calculation of the yield of SOA product mass from the emissions inventory VOC's, based on the VBS model, and the treatment of this mass as a primary aerosol emission, similar to the POA. Utilizing the similarity in microphysical and optical properties of OA and sulfate, the model carries POA and SOA together with sulfate as aforementioned "anthropogenic and biogenic fine". This approach has some obvious shortcomings, but it carries minimal computational cost and has much improved the simulation of AOT, especially the model bias and correlation with AERONET over India, China and Eastern United States.

2.2.7 Biomass Burning Smoke

Biomass burning has a wide coverage globally, from the tropics to the high latitudes, and it significantly impacts the total light absorption budget (Bond et al., 2013). Unlike other aerosol sources that are meteorologically driven (e.g., dust and sea salt) or prescribed in a seasonal or monthly inventory (e.g., pollution), smoke emissions have significant variability that hinders easy parameterization. Configuring the NAAPS model with biomass burning aerosols as a separate species permits explicit hypothesis testing about the sources, sinks, and optical properties of these aerosols. Operational NAAPS has adopted the satellite active fire hotspot based approach through the Fire Locating and Modeling of Burning Emissions (FLAMBE1.0; Reid et al., 2009; Hyer et al., 2013). The model converts the smoke emission to total mass injected by multiplying by the fire size. This value is then divided by the area of the grid cell and the fire duration to create a flux as an hourly input to the model. FLAMBE can use satellite fire products from either geostationary sensors, which offer faster refresh rates and observation of the full diurnal cycle, or polar orbiters, which have greater sensitivity. Polar orbiting satellites have significant biases not only in their daily sampling pattern, but also additional artifacts from day to day shifts in the orbital pattern (e.g., Heald et al., 2003, Hyer et al., 2013). Over the reanalysis period, multiple changes in the geostationary constellation posed a challenge for consistency of the smoke source function. Therefore, a polar-only version of FLAMBE was created for the reanalysis.

Given that the NAAPS reanalysis coincides with the NASA EOS system, MODIS-based fire products and emissions are applied. MODIS orbits have a 16-day repeat cycle, with daily coverage of the globe excepting small gaps between orbits at the equator. Areas that are not covered one day are centered on the orbit the next. The Fire Inventory from NCAR (FINN, Wiedinmyer et al. 2011), which is also based on MODIS active fire detections, uses a 3-day moving average to account for gaps and orbital variations. After testing multiple coverage corrections, we found that for the reanalysis a simple two-day maximum (previous day and present day) fire signal largely mitigated orbital effects and thick clouds in a

tractable way. This correction is consistent with the self-sustained nature of regional fire emissions, and further improves upon the scores presented in Reid et al. (2009).

Smoke injection height combined with boundary layer mixing has a strong influence on how smoke is dispersed. Most plumes are observed as constrained within the planetary boundary layers, especially within the tropics and subtropics (Tosca et al., 2011, Campbell et al., 2013). Large boreal fires can pump smoke to higher altitudes, though these fires constitute only a very small portion of the total fires and global budget of AOT (Fromm and Servranckx, 2003; Kahn et al., 2008). In NAAPS, smoke is injected into the bottom four layers of the model, which is approximately the bottom 400 m of the model. Tuning of injection height to match observed aerosol vertical profiles is feasible in regional studies (e.g., Wang, et al., 2013). However, we use the uniform injection height in NAAPS, considering that boundary layer processes generally quickly mix aerosols well within the boundary layer or below the models significant inversion height to produce a result similar to the observations of Kahn et al. (2008).

2.3 AOT assimilation

The core of the NAAPS AOT reanalysis is AOT assimilation using the Navy Atmospheric Variational Data Assimilation System for Aerosol Optical Thickness (NAVDAS-AOT; Zhang et al., 2008). NAVDAS-AOT is a system that, by default, assimilates quality-controlled two-dimensional MODIS AOT at 550 nm into NAAPS. It additionally has the ability to perform three-Dimensional (3DVAR) assimilation using the Cloud Aerosol Lidar with Orthogonal Polarization (CALIOP) product of Campbell et al. (2010) in Zhang et al. (2011). The main impact of 3DVAR assimilation is redistribution of aerosol mass vertically, while conserving the total column mass and AOT. CALIOP data is available for only part (2006-2013) of the reanalysis period, therefore, in this first study we perform 2DVAR AOT assimilation only.

2.3.1 Formulation of NAVDAS-AOT

The NAAPS prognostic variable is the 3D aerosol mass concentration. A 2DVAR approach is adopted for AOT assimilation simply because AOT retrievals from MODIS and MISR are a column-integrated aerosol optical property. The 2DVAR AOT assimilation is realized through three steps:

(1) Convert NAAPS mass concentration AOT:

$$\tau_{b_\lambda} = H_{m\_\tau}(C_m) + \epsilon_{b\lambda} \quad , (13)$$

where $\tau_{b\lambda}$ is the background (prior analysis) AOT vector, C_m is the NAAPS mass concentration, and H_{m_τ} is the forward operator that represents the conversion of NAAPS mass concentration to AOT. $\varepsilon_{b\lambda}$ is the error in $\tau_{b\lambda}$ introduced by the H_{m_τ} operator;

(2) 2-D variational assimilation of the AOT field:

$$\tau_{a\lambda} = \tau_{b\lambda} + P_b H^T [H P_b H^T + R]^{-1} [\tau_{o\lambda} - H(\tau_{b\lambda})] \quad , (14)$$

where $\tau_{a\lambda}$ is the analysis AOT vectors, $\tau_{o\lambda}$ is the observation AOT vector, and H is the observation operator that represents any necessary spatial and temporal interpolations from the background to observational space. P_b and R are the background error covariance and observational error covariance matrices, respectively. The analysis field can be considered as the background ($\tau_{b\lambda}$) plus a correction term (the second term on the right hand side of Eq. 14), which is the difference between the observation and background vectors weighted by the ratio of background error covariance matrix to total error covariance matrix in the observational space;

(3) Convert the analysis AOT vectors to NAAPS mass concentration:

$$C_m = H_{\tau\_m}(\tau_{a\lambda}) + \epsilon_m \quad , (15)$$

where H_{τ_m} is the backward operator that performs the conversions from AOT to NAAPS mass concentration. In the backward operation, a scaling factor is applied to the vertical profile of aerosol mass based on the ratio of the AOT correction and background AOT, while keeping the hygroscopic

446 growth rate (Eq. 6) unchanged. ε_m is the error in C_m introduced by the H_{τ_m} operator. Both ε_m and $\varepsilon_{b\lambda}$ can
447 be transformed as part of the error term of $\tau_{b\lambda}$, which is assumed to be zero for this study.

448

449 2.3.2 Observational and background model error covariance matrices

450 Both observational and model errors could contain systematic bias, either of which could be
451 removed or minimized through pre-processing. For example, our quality assurance (QA) and quality
452 control (QC) methodology (Section 2.3.3) attempts to remove systematic bias as much as possible from
453 the AOT observations. Likewise the tuning process described in Section 2.4 attempts to remove
454 systematic bias from the model background. Thus, both model background and observations are
455 assumed to be unbiased in NAVDAS-AOT.

456 In NAVDAS-AOT, observational errors are assumed to be uncorrelated. Thus, only observational
457 error variances are needed. The error variances for the gridded satellite AOT data are computed by the
458 summation of instrumentational error variances and sample error variances (Zhang et al., 2008). The
459 instrumentational error variance is estimated through the comparison of satellite and ground-based
460 sun-photometer data as shown in Zhang and Reid (2006) and Shi et al. (2011a) for MODIS "Dark Target",
461 and Shi et al., (2014) for MISR aerosol products. The sample error variance measures the variance in the
462 gridded mean (or the representative error variance). For a 1^o latitude by 1^o longitude grid, the sample
463 error variance is derived by the spatial variance of the AOT data of the grid divided by the number of
464 observations that are used in computing the gridded mean value.

465 The background error covariance is computed for any given two horizontal model grid locations
466 *m* and *n* based on the following equation

467 $$P_b^{mn} = [S_b^m]^{1/2} C_b^{1/2} [S_b^n]^{1/2} \quad , (16)$$

where P_b^{mn} is the background error variance for horizontal grid locations of *m* and *n*. S_b^m and S_b^n are the model error variances at grid locations *m* and *n*, respectively. C_b is the horizontal background error correlation between the two grid locations. Similar to observational error variances, model error variances are also estimated using ground based sun-photometer data, and the values are reported in Zhang et al. (2008). The C_b values are computed using the second order auto-regressive (SOAR) approximation (Daley and Barker, 2001),

$$C_b(m,n) = (1 + R_{mn} / L\ ) \exp(-R_{mn} / L\ ) \quad . (17)$$

Here R_{mn} is the great circle distance between *m* and *n*. *L* is the horizontal error correlation length. The horizontal error correlation length is estimated through evaluating the differences in AOT between satellite observations and 6-hour model forecasts as a function of horizontal distance. *L* is set to 200 km for this study based on Zhang et al. (2008).

2.3.3 Input data for NAVDAS-AOT and its preprocessing treatment

The basis of input data for the reanalysis is operational MODIS Collection 5 AOT (Levy et al., 2007; 2010; Remer et al., 2005; 2008) and Multi-angle Imaging SpectroRadiometer (MISR) AOT products (Martonchik et al., 2009, Kahn et al., 2009, Kahn et al., 2010). MODIS Deep Blue for Collection 5 is not used here due to bias issues, but it is expected that improvements in Collection 6 will be made and the data could be assimilated (Shi et al., 2013). Extensive quality assurance (QA) and quality control (QC) procedures applied to the MODIS C5 AOT are conducted as described in Zhang et al. (2006) and Shi et al. (2011a) for over water and Hyer et al. (2011) for over land. These QA/QC procedures are especially important for this application, because the analysis must be heavily weighted to the observations to allow assimilation for correct for errors such as missing dust and smoke sources. Under these

circumstances, the impact of noisy data is large and proper filtering and correction of data is critical. QA/QC procedures implemented for MODIS and MISR AOT include a) strict checks for removal of possible cloud contamination, b) corrections for the lower boundary condition, such as wind speed to correct for white caps and specular reflection over water and surface albedo over land, and c) aerosol micro-physical corrections based on derived fine mode fraction over water and regionally over land. This strict quality assuring and quality control procedure is necessary to remove outliers and minimize erroneous aerosol features in MODIS that would adversely impact the model and propagate through the system. Currently, the total global data loss through screening of MODIS is about 40%, with a reduction of absolute errors of 10–30% over water (Zhang et al., 2006; Shi et al., 2011a). Over-land, the QA/QC procedures reduce data volume by ~60% and improve the global fraction of MODIS AOT within 0.05 ± 20% of AERONET (Hyer et al., 2011). The data are aggregated into a 1^{o} x1^{o} grid that matches the model resolution where additional buddy checks are applied.

A benefit of a reanalysis is that observations that are not timely enough to be incorporated into an operational run can be utilized. Thus, while MODIS products are used in all versions of NAAPS, for the reanalysis we can make use of MISR. Though narrower in swath than MODIS, and thus providing less relative coverage, MISR has two key benefits. First, MISR is on Terra and its imaging swath is in the MODIS sun-glint region. Hence, MODIS plus MISR completes the MODIS swath with full coverage. Second, the MISR over-land algorithm has an advantage over retrievals conducted with other sensors in its handling of the lower boundary condition, provided that AOT<0.8. In particular, there are large spatially-correlated discrepancies between the retrieved MODIS and MISR AOT in regions of high albedo as a result of deficiencies in the MODIS lower boundary condition (Shi et al., 2011b). Notable regions of discrepancy between MODIS and MISR include the Andes Mountains, Saharan Africa, the Arabian Peninsula and Central Asia (Shi et al., 2011b). Further, MISR can retrieve AOT in desert region at high efficacy where the operational MODIS Collection 5 “Dark Target” products cannot, thus providing

514 further coverage in desert regions. Quality-assuring (QA) and quality control (QC) procedures, including
515 the use of MODIS cloud mask products to reduce cloud contamination in MISR data sets and applying
516 various quality checks and empirical corrections on MISR Level 2 aerosol products, are conducted to
517 generate data assimilation (DA) quality data sets (Shi et al., 2011c, 2014). Then the data are aggregated
518 into a 1^{o} latitude by 1^{o} longitude grid.

519 Data assimilation using NAVDAS-AOT is used to produce a new analysis after every six hours of
520 NAAPS integration time. The MODIS and MISR Level 2 aerosol products are typically acquired in a 6-hr
521 range centered on the nominal valid time of the analysis (i.e., 0, 6, 12 and 18 UTC) from NASA data
522 servers. Then QA/QC processes convert MODIS and MISR level 2 data into filtered, corrected, and
523 aggregated AOT observations with associated uncertainty estimates for assimilation in NAVDAS-AOT.
524 After QA/QC processes, the general pattern of data coverage from MODIS and MISR for each
525 assimilation cycle is shown in Fig. 1. The observed geographic pattern is attributed to the fact that
526 MODIS and MISR AOT retrievals are limited to daytime and a limited range of sun-sensor geometries.
527 The longitudinal range for which MODIS and MISR data is available in a given assimilation cycle is limited
528 because Terra and Aqua are in sun-synchronous orbits with equatorial overpass time of 10:30 and 13:30
529 local solar time, respectively.

530 For the MODIS sensors, overlapping coverage between Terra and Aqua over the 6-hr data
531 acquisition period does occur and a mean of Terra and Aqua weighted to the number of Level 2
532 retrievals from each sensor. The contribution of each individual sensor to the total volume of the MODIS
533 DA quality data is about 50% on average, although this number is highly variable on the 6-hourly basis,
534 with the variability depending on the observability of the sensors (e.g., cloudy vs. non-cloudy, land vs.
535 ocean, etc…). Because of its narrower swath compared to MODIS, the data volume of the MISR DA-
536 quality data is only about 22% on average of that of MODIS. Approximately half of the MISR DA-quality

data overlaps with MODIS. When overlapping of MISR and MODIS 1°x1° 6-hourly DA-quality data occurs, the mean of the two is taken for final assimilation purpose.

The seasonal geographic distribution of the total number of 6-hourly 1°x1° fused MODIS and MISR DA quality AOT data averaged over 2003-2013 is shown in Fig. 2 (left column). Areas with high cloud coverage, including the ITCZ and the subtropical stratus cloud deck regions, have relatively less data. In the polar regions, cloud contamination often exists in satellite-retrieved AOT data, leading to elevated AOTs. The Southern Oceans is an example of cloud-enhanced MODIS AOT, for instance (Toth et al., 2013). As a result, high-latitude AOT data are filtered out in the QA/QC process. The cut-off latitudes for AOT data to be assimilated are 40°S over water for the southern hemisphere and 80°N for the northern hemisphere. In addition, because MODIS and MISR AOT observations are only available during daylight, and thus there are no observations during polar nights, this results in more data counts in boreal summer than in boreal winter. Fig. 2 also shows that areas with bright desert (e.g., Saharan Africa, the Arabian Peninsula and Central Asia), or snowy/icy surfaces (e.g., Andes Mountains, Greenland and high latitude in boreal winter) have relatively less data to be assimilated, as these regions are mainly filled in by MISR retrievals that have a revisit time of seven days on average rather than a revisit time of one day by MODIS.

The start date of the reanalysis is 1 January 2003, based on the availability of the observational data used in the reanalysis. Terra MODIS and MISR AOT data are first available in March, 2000, and Aqua MODIS AOT is first available in July 2002. An additional consideration is CMORPH precipitation data, which is used to replace model precipitation within the tropics, is not available until December 2002. Since the required spin-up time for the aerosol model is one month, the reanalysis starts at 1 January, 2003. Figure 3 shows the time evolution of 6-hourly data counts of the global MODIS, MISR and the fused 1°x1° grid DA quality AOT in dots and their center-point thirty-day running average in solid lines. Throughout the reanalysis time period (2003-2013), the data counts of the DA quality data are relatively

561 stable, despite small dips in December 2003 in both MISR and MODIS and October 2008 in MISR due to
562 the upstream data being unavailable. The data count of the fused MODIS and MISR DA quality data is
563 about 3800 during boreal summer and 2400 during boreal winter, on average. This essentially follows
564 the seasonal variation of the MODIS DA quality data count, which makes up about 80% of the total fused
565 MODIS and MISR DA quality data. Half of the remaining 20% is attributed to MISR alone and half is
566 attributed to the overlapping MISR and MODIS DA quality data. The seasonal variation of data volume is
567 mainly related to the fact that more AOT data are discarded for the southern hemisphere high latitudes
568 than the northern hemisphere high latitudes as a result of cloud contamination, and no observations are
569 available during polar nights (Fig. 2).
570
571 2.4 Tuning studies

572 While AOT data assimilation from sensors such as MODIS and MISR improves NAAPS
573 performance (Zhang et al., 2014), the natural NAAPS model performance is equally important for
574 generating a final reanalysis product that aims to match observations. Previous studies have shown that
575 aerosol source functions, inherent within the natural runs, are one of the largest uncertainties with
576 respect to aerosol modeling of AOT (e.g., Kinne et al., 2003). As a result, a series of source-tuning
577 exercises have been carried out on the natural model, using AERONET and satellite AOT observations for
578 constraint. The tuning exercises consisted of running the model multiple times while iteratively adjusting
579 model source and sink parameters. Smoke emissions and dust erodibility, for regions as shown in Fig. 4
580 with some additional divisions as shown in Table S1, were tuned by iterative comparison between
581 NAAPS model output without data assimilation and AERONET data, as described in Section 2.4.1.
582 Emissions for some regions not covered by AERONET, as well as aerosol sink parameters, were
583 constrained using the AOT assimilation correction field as described in Section 2.4.2. A list of the
584 corrections applied is given in Table S1. The range of variation in optical properties of dry aerosols

585 reported in the literature (e.g., Hess et al., 1998; Kinne et al., 2003) is small compared to other
586 uncertainties, therefore we adopted the optical properties described in section 2.2.2 without additional
587 tuning.

588 2.4.1 Tuning of aerosol sources with AERONET

589 The AErosol RObotic NETwork (AERONET, http://aeronet.gsfc.nasa.gov), a ground-based global
590 scale sun photometer network, has been providing high-accuracy measurements of aerosol properties
591 since the 1990s (Holben et al., 1998; Holben et al., 2001). AERONET instruments measure sun and sky
592 radiance at several wavelengths, ranging from the near ultraviolet to near infrared during daytime. It is
593 often used as the primary standard for validating satellite products and model simulations (e.g., Kahn et
594 al., 2010; Levy et al., 2010; Colarco et al., 2010). Since there are no AERONET data at 550 nm,
595 measurements from multiple wavelengths (380 nm to 1020 nm) were used to estimate both fine and
596 coarse mode AOTs at 550 nm, based on the Spectral Deconvolution Method (SDA) of O'Neill et al. (2001,
597 2003). Extracted fine and coarse mode AOTs from AERONET AOTs are then compared to ABF plus
598 smoke and sea salt plus dust, respectively. The SDA product has been verified using in situ
599 measurements (Kaku et al., 2014) and has been shown to be able of capturing the full modal
600 characteristics of fine and coarse particles while avoiding the uncertainties that come from using static
601 diameter thresholds, at 0.8 or 1.0 μm for example. Further, the SDA has also been shown to eliminate
602 any potential cloud bias in fine mode AOTs from AERONET (Chew et al., 2011), although thin cirrus
603 contamination into the coarse model AOT can still be problematic in some regions such as Southeast
604 Asia and Equatorial Africa (Chew et al., 2011; Huang et al., 2011).
605 Only cloud-screened, quality-assured Level 2 AERONET data are used in this study (Smirnov et al.,
606 2000), and the sites are marked with black dots in Fig. 4. Within the reanalysis time period, nearly 600
607 regular sites provided valid observational data. AERONET Distributed Regional Aerosol Gridded

608 Observation Networks (DRAGON) observations are concentrated over a small area and a short period of
609 time, and they are excluded from this study to avoid the effect of uneven sampling on the results from
610 the statistical analysis. Spatially, the 1x1 degree grids in which the AERONET Level 2 data fall within are
611 identified, and the model AOT is sampled from these identified model grids. Temporally, AERONET Level
612 2 data are binned into 6-hourly intervals centered at the model synoptic output times of 00, 06, 12 and
613 18 UTC and then averaged within the bins. The model AOT at 550 nm is sampled consistently with
614 AERONET: we extract the model AOT at a site using only times when AERONET had measurements. A
615 second approach is tested, in which the model data is interpolated onto AERONET observation times.
616 Validation results from the two methodologies are similar.
617 Empirical regional tuning of smoke and dust emissions is based on the fine and coarse mode
618 AOT comparisons with AERONET. The globe is divided into sixteen regions, as shown in Fig. 4, each
619 having their own distinct aerosol characteristics. For example, South America, South Africa, Peninsular
620 Southeast Asia, and Insular Southeast Asia have a prevailing smoke aerosol species during burning
621 seasons, while North Africa and Southwest Asia are dust dominated. East Asia and Indian Peninsular
622 have mixed dust and pollution. Regional emission tuning factors were generated by using the regional
623 bias and slope of the linear regression between pair-wise NAAPS and AERONET AOT. This is done for
624 2009-2011 when AERONET data is more abundant than earlier years. Seasonally, data are grouped into
625 the boreal winter/spring (December to next-May) and boreal summer/fall (June to November) time
626 periods. These bi-seasonal temporal stratifications account for the major monsoonal and climatic shifts
627 in the atmosphere while preserving major aerosol seasons such as, for the boreal summer/fall, the
628 August-October biomass burning seasons in South Africa, South America, and Maritime Continent, the
629 June-August African dust season, and the U.S. and European summer haze seasons.
630 Regional emission factors, in the form of linear scaling factors applied to the original source
631 functions for smoke and dust, are derived for each aerosol active season for the three years. For a single

tuning factor, it differs slightly from year to year and season to season to a certain range. An average over the six seasons is taken to generalize this tuning factor for the reanalysis. The model is then run using the corrected emissions and the results are validated regionally against AERONET to determine whether the tuning improved bias, correlation, and root mean square error (RMSE). Additionally, the fine/coarse mode AOT time series of NAAPS and AERONET are reviewed for each site in the region to ensure the tuning is sensible. This process is repeated iteratively to refine the tuning. In the supplemental Table 1, the values of the regional multipliers for smoke emission based on the two-day maximum MODIS-only FLAMBE data base are listed. Also provided are the regional multipliers for soil erodibility, which are used to modify the dust source (Ginoux et al., 2001). The tuning factor for soil erodibility changes twice over the 11 years to accommodate the land surface parameterization changes in the meteorological analysis.

2.4.2 Tuning with AOT assimilation correction/increment field

The total number of operational AERONET sites has grown to over 300 in recent years. However, the network's global coverage is uneven with the majority of sites located over land where they are easily accessible. The available AERONET data is often not representative of major aerosol impact regions, and it does not optimally sample for the biases that remote sensing products may have (Shi et al., 2011b). In particular, open oceans have few AERONET sites.

In regions with sparse AERONET data coverage, aerosol sources and parameters, such as sedimentation and dry deposition for ocean regions, are tuned using satellite AOT assimilation correction/increment fields. The monthly means of the daily AOT corrections (i.e., the difference between the assimilation posterior and the model prior) are a good indicator of the model performance globally. The correction maps can be used to quickly identify geographic regions where the model succeeds or does poorly. A region in which the data assimilation consistently suppresses aerosol mass

could indicate a region with excessive aerosol emissions, or deficient removal, with the assumption that aerosol transport has much smaller uncertainty.

Since satellite products have uncertainties, especially over land, we rely on source corrections inferred from AERONET except where there are no representative sites close to the known source area (e.g., southern African biomass burning region). Over the ocean where AERONET has only a few sites globally, satellite data assimilation plays an irreplaceable role, not only because of the good spatial and temporal coverage of satellite AOT data, but also because of its much smaller uncertainty compared to the over-land AOT product (Hyer et al., 2011). Dust dry deposition velocity over water is tuned based on the AOT correction over the tropical Atlantic where African continent dust outflow is located, and is set to 0.001 m s^{-1}. To minimize the AOT correction over global ocean, especially high-latitude regions where surface wind is large, we also update the sea salt dry deposition velocity over water from a constant to a function of surface wind speed following Eq. (8). This effectively reduces the negative AOT correction over high-wind regions. This approach does not account for possible sources of error, including sea salt emission parameterization, biases in surface wind that drives emission and biases in boundary layer relative humidity that affects hygroscopic growth of the sea salt particles. In particular, our approach assumes that meteorological fields are correct, and implements correction solely to the uncertain parameters of aerosol sources and sinks.

3.0 Reanalyzed Aerosol Optical Thickness

In this section, we focus on evaluating the reanalysis AOT at 550 nm apportioned into fine and coarse mode contributions. The sum of the fine and coarse mode AOTs constitutes the total AOT. These are what we consider the key reanalysis output variables. Dust and sea salt are considered coarse-mode aerosols and the ABF and smoke aerosols are considered fine-mode aerosols, given the simple microphysics of the NAAPS model. Seasonally, the boreal winter/spring (December to next-May, ie.,

DJFMAM) and boreal summer/fall (June to November, ie., JJASON) time periods are investigated. When performing bi-seasonal long-term averaging, we use only data in June 2003-May 2013 time period, so that each individual month has an even weighting.

3.1 Global distribution of AOT and seasonal variability

The bi-seasonally averaged total, fine, and coarse mode AOTs at 550 nm for the 2003-2013 time period are presented in Fig. 5. Results are shown for the reanalysis and a parallel model run using tuned source and sink parameters but without AOT data assimilation. The fused MODIS-MISR DA-quality AOT for the same time period are shown in Fig. 2 (right column) for comparison. The total AOTs for both the NAAPS runs with and without AOT data assimilation look very similar to the fused DA-quality MODIS-MISR AOT. Prominent fine mode features include pollution over East Asia and India, as well as biomass burning in South Africa, South America and the Maritime Continent in JJASON. Distinguishable coarse mode features include Saharan dust, Arabian and central Asian dust, and the circumpolar sea salt belt over the Southern Ocean. For DJFMAM, the total AOTs for both the NAAPS runs with and without AOT data assimilation also look very similar to the fused DA-quality MODIS-MISR AOT. As for the fine-mode AOT, in addition to the year-round pollution over East Asia and India, biomass burning in central Africa and Peninsular Southeast Asia shows up for the DJFMAM season. As for the coarse-mode AOT, dust over Sahara, Sahel, Arabian Peninsula and East Asia are clear and the circumpolar sea salt belt over the southern ocean is persistent. The seasonal global average total AOTs for over-ocean and over-land from the reanalysis are also similar to those of the fused DA-quality MODIS-MISR AOT. The NAAPS run without AOT assimilation has slightly higher global average total AOTs for over-ocean and over land, mainly attributed to higher fine mode AOT averages.

The similarity between the NAAPS runs with and without AOT data assimilation implies that the AOT correction by the data assimilation process is small and the whole model tuning process is effective. The resemblance between the reanalysis (NAAPS with AOT data assimilation) AOT and the fused MODIS-MISR AOT indicates that the data assimilation system works well in adjusting model fields to the closest observations. In this study, the model tuning process is considered equally as significant as the AOT data assimilation in influencing the final reanalysis. As the DA-quality satellite AOT data can reflect relatively small global coverage (Fig. 1, Fig. 2), areas not covered by the DA-quality satellite AOT would be highly impacted by the natural model (NAAPS without data assimilation). More details on the impact of tuning versus the DA on the model performance are provided in Appendix.

For this type of comparison (Fig. 5), which is done with all available model and satellite data, we should also expect some difference between the satellite retrievals and the reanalysis, resulting from contextual biases in satellite products such as clear sky biases (Zhang and Reid, 2009). Satellite retrievals for AOT mainly occur over clear sky, while the model depicts both clear and cloudy situations. Aerosol conditions can be very different between clear and cloudy sky, which is often associated with weather systems. For example, during the South America and Africa burning season (corresponding to JJASON), the southeast outflow regions from the southeast coast of the continents into the southern oceans are found to have lower seasonal average AOT for clear sky compared to cloudy/all sky, as smoke plumes are often transported along with the cloud system (Zhang and Reid, 2009). This clear sky bias is also discernable comparing MODIS AOT and the reanalysis AOT (Fig. 2 and Fig. 5).

3.2 Validation with AERONET

For validation purposes, we use the quality-assured AERONET Level-2 product. The reanalysis AOTs are compared with AERONET 6-hourly total, fine and coarse mode AOTs at 550 nm.

3.2.1 Global overview

Over the reanalysis period (2003-2013), the number of AERONET observations that can be paired with model data gradually increases with time (Fig. 6a). The daily volume of global 6-hourly AERONET data has more than doubled in 2012 compared with 2003. The data count in 2013 decreases slightly due to the long processing time required for validating AERONET Level 2 data (instruments need to be removed from the field and recalibrated (Smirnov et al., 2000)). As there are more AERONET sites in the northern hemisphere than in the southern hemisphere and AERONET measurement only occurs during daytime, there are more AERONET observations during boreal summers than winters. Polar and high-latitude sites have few or no observations in winter, which raises a temporal sampling issue in validation for these regions. AERONET sampling also covaries with the seasonal AOT assimilation cycle, as high-latitude regions are less influenced by AOT assimilation during the wintertime.

Despite the uneven seasonal sampling, the ninety-day running average of the root mean square error (RMSE) of reanalysis AOTs is quite stable throughout the reanalysis time period (Fig. 6b), at around 0.1 for both fine and coarse mode AOTs and 0.14 for the total AOTs. Daily average RMSE can occasionally exceed 0.4.

Figure 7 provides the comparison of the pair-wise 6-hourly reanalysis AOT and AERONET AOT for all of the available global sites during the reanalysis time period. The normalized data density is shown in color. AOT data from AERONET and the reanalysis are binned at a resolution of 0.01 and density of each bin is colored relative to the maximum density in the sample. Also shown are the basic statistics of the comparison: the total number of stations and the 6-hourly observations, bias, root-mean-square error (RMSE), square of the Pearson correlation coefficient (r^2), and the linear regression parameters of the Theil-Sen method (Theil, 1950; Sen, 1968). The slope of the Theil-Sen linear regression is defined as the median of the slopes determined by all pairs of two-dimensional sample points. It is a robust linear

748 regression that is insensitive to outliers and more accurate than the least-squares regression for
749 potentially skewed data. For reference, also shown is the linear least square regression line, which is
750 more sensitive to outliers.

751 For both JJASON and DJFMAM, the global reanalysis fine-mode AOT has a small positive bias of
752 slightly less than 0.01, while the coarse-mode AOT has a negative bias close to -0.02. The resulting bias
753 for total AOT is -0.01. It is noteworthy that perhaps a portion of the AERONET coarse mode bias is due to
754 cirrus contamination (Chew et al., 2011), which will be mitigated in the next major revision of AERONET
755 data. The RMSE values for both fine and coarse mode 6-hourly AOTs are ~ 0.1, except that the RMSE of
756 the coarse AOT is a little higher (0.11) during DJFMAM and a little lower during JJASON (0.08). The
757 seasonality of RMSE for coarse mode AOT is more apparent than that of the fine mode AOT, which is
758 consistent with Fig. 6. RMSE for the total AOT is 0.14 for both seasons, consistent with Fig. 6 as well. r^2
759 is close to 0.65 for fine mode AOT and close to 0.61 for coarse mode AOT for both seasons. r^2 for the
760 total AOT is about 0.7, which is slighter better than the individual fine/coarse mode AOTs. The slope of
761 the Theil-Sen regression lines is greater than 1 (around 1.3) for the fine mode AOT, less than 1 (around
762 0.8) for the coarse mode AOT, and very close to 1 for the total AOT for both seasons. All of the above
763 statistical numbers indicate that the fine mode AOT has a small high bias while the coarse mode AOT has
764 a small low bias on average and globally. There is little seasonal difference in the mode statistics (fine,
765 coarse and total modes) for the whole globe.

766 As monthly data is often used in climate studies, we also evaluate the reanalysis monthly
767 averaged AOTs (Fig. 8). Monthly averages are obtained only when the total number of 6-hourly
768 AERONET data exceeds ten. For validation purposes, the monthly average reanalysis AOT is calculated
769 based on the available 6-hourly data that can be paired with AERONET data. With the high frequency
770 signals (e.g., daily variability) smoothed out, the monthly average exhibits a better match with AERONET

771 data over all. For both seasons and all modal AOTs, the monthly averages in the scatter plots are more
772 aligned with the 1:1 lines, RMSE is roughly 50% lower (0.07 for total AOT, 0.05 for fine and coarse mode
773 AOTs), and r^2 about 0.2 higher on average (with a maximum of 0.90 for the total AOT in DJFMAM and a
774 minimum of 0.74 for the coarse AOT in JJASON). While absolute bias is unaffected by averaging, there
775 appears a slope bias in linear regression results. Sites that may have a low background punctuated by
776 severe events will appear in the regression differently from sites with a consistent but high background.
777 This results in slope bias in regression of monthly averaged AOT values, demonstrating the dangers of
778 applying monthly mean data to downstream calculations such as radiative forcing. Such calculations
779 need to be conducted at the finest spatial and temporal scales achievable, with accounting for
780 resolution effects.

781 Figure 9 shows the cumulative distribution function (CDF) of AOT errors compared with
782 AERONET for total, fine and coarse AOTs, respectively, using 6-hourly data. As a reassurance, the CDF of
783 AOT errors compared with MODIS and MISR DA quality data is also shown. Because the seasonal
784 differences for the global validation statistics are small, the two seasons are combined for the CDF
785 analysis. As expected, the reanalysis total AOT is in good agreement with MODIS and MISR DA quality
786 AOTs, though slightly less agreement with MISR than MODIS is found as the relative number of MISR
787 data involved in AOT assimilation is much less. More than 95% of the reanalysis total AOT has an AOT
788 error falling in the AOT error range of [-0.05, 0.05] compared with MODIS or MISR. The reanalysis AOT
789 has larger errors with respect to AERONET. The crossing points of the CDF curves and the zero AOT error
790 line (and the -0.1/+0.1 error lines) show that about 35% fine mode AOT has a low bias (4% with error
791 less than -0.1) and the other 65% has a high bias (6% with error greater than 0.1) compared to AERONET.
792 For coarse mode AOT, about 60% has a low bias (7% with error less than -0.1) and 40% has a high bias (2%
793 with error greater than 0.1). For the total AOT, about 44% has a low bias (10% with error less than -0.1)

794 and 56% has a high bias (8% with error greater than 0.1). On average the fine AOT has a slight high bias
795 and the coarse AOT has a slight low bias, which is consistent with the scatter plot result (Fig. 7).

796 3.2.2 Regional Evaluation

797 Figures 10, 11, and 12 show box-whisker plots of the pair-wise comparisons of regional
798 reanalysis 6-hourly modal AOT vs AERONET: percentiles marked in the plots are 95%, 90%, 75%, 50%,
799 25%, 10% and 5%, for the regions defined in Fig. 4 for 2003-2013. Also shown are regional mean AOTs
800 designated by a diamond for AERONET and "+" for the reanalysis. Detailed statistics associated with Fig.
801 10-12 (including separation into two seasons) are provided in the supplemental material. These include
802 seasonal means and medians of the reanalysis and AERONET, along with reanalysis bias, RMSE, r^2, Theil-
803 Sen linear regression parameters and number of valid data points for each region and the globe.

804 In general, the reanalysis follows the regional variation found in AERONET for fine-mode, coarse-
805 mode and total AOTs. For the fine mode AOT, the reanalysis matches well with AERONET with respect
806 to the regional means, medians, and variance. However, the results vary by region (Fig. 10). The
807 regional means and medians are the same or slightly larger than those of AERONET for all regions,
808 except East Asia and insular Southeast Asia, where the means are smaller than AERONET. The high AOT
809 regions are the developing East Asia, Indian subcontinents, Peninsular and Insular Southeast Asia. These
810 regions also have the highest RMSE values varying between 0.15 and 0.2, while RMSE values of other
811 regions are all below 0.1. The low bias in mean fine mode AOT in East Asia and insular Southeast Asia is
812 mostly due to the model's inability to capture the magnitude of large fine aerosol events (e.g. extreme
813 pollution and biomass burning events). The correlation coefficients (r^2) of most regions fall between 0.5
814 and 0.9. The best performing region is South America, whose r^2 is greater than 0.8, indicating the
815 reanalysis captures the temporal variation in fine mode aerosols, which are attributed mostly to biomass

816 burning smoke. Regions with worse r^2 include West Continental United States (W. CONUS), North Africa,
817 SW Asia and insular Southeast Asia, with r^2 around 0.4-0.5.

818 The coarse mode AOT, overall, agrees less well with AERONET than the fine mode AOT with
819 respect to the regional means, medians, variances and correlations (Fig. 11). Many regions have
820 generally very low coarse AOT; RMSE for these regions will be low, but r^2 will also be low due to the
821 small dynamic range. The most prominent high coarse mode AOT regions are the dusty North Africa and
822 Southwest Asia domains. The moderate coarse mode AOT regions are dust-influenced Indian
823 subcontinent, East Asia and Central America. These regions have relatively large RMSE (between 0.1 and
824 0.2), except central America (<0.1), compared to other regions (<0.1). Except for Southwest Asia, the
825 oceanic region, North America boreal, W. CONUS and Australia, where the reanalysis mean coarse mode
826 AOT is comparable to that of AERONET, other regions show mean low biases. The low bias, relative to
827 the mean AOT, is generally small, except for Peninsular and insular Southeast Asia. The bias over these
828 regions is attributed largely to the known thin cirrus contamination in AERONET L2 data (Chew et al.,
829 2011; Huang et al., 2011). Thin cirrus cloud is a significant challenge for sun photometer aerosol optical
830 thickness measurement, as it is easily miscategorized as coarse-mode aerosols by the instrument. The
831 persistent occurrence of high thin cirrus cloud over these regions elevates the mean coarse mode AOT
832 and thus the mean total AOT substantially. For example, at Singapore, a representative site for the
833 insular Southeast Asia, 34% of AERONET L2 AOT data is found to be coincident with Micro-Pulse Lidar
834 Network (MPLNET)-observed cirrus clouds (Chew et al., 2011). The estimated range of positive AOT bias
835 in AERONET L2 data over Singapore, due to unscreened cloud presence, ranges from 0.03 to 0.06. Taking
836 this estimated AOT bias of AERONET L2 data into account, the reanalysis coarse-mode AOT would be
837 very close to reality. A similar situation exists for the peninsular Southeast Asia, based on the estimated
838 cirrus cloud contamination in AERONET data at the regionally representative Pimai, Thailand site (Huang
839 et al., 2011).

840 The correlation coefficients r^2 of the coarse mode AOT are less than those of the fine mode AOT
841 for most regions, except for north Africa, SW Asia, Europe-Mediterranean and India, which have strong
842 dust influence. Insular and Peninsula SE Asia have the worst correlations as expected, mostly because of
843 the cirrus cloud contamination in AERONET data. Other regions which have small AOT variations (e.g.
844 dynamical data range less than 0.1) tend to have small r^2 s, e.g., north American Boreal and W. CONUS.

845 The total AOT, which is the sum of the coarse-mode AOT and fine-mode AOT, has a validation
846 feature that combines the validation properties of the two AOT modes (Fig. 12). The regional variation
847 of total AOT follows that of AERONET well. The variance of the reanalysis for each region is smaller
848 overall than that of AERONET, suggesting the difficulty in capturing extreme events with the model and
849 assimilation system and a tendency to underestimate the magnitude of extreme events and
850 overestimate in very clean conditions. A smaller AOT variance is known to be a typical model behavior
851 among aerosol models (Kinne et al., 2006; Sessions et al., 2015) and is a persistent challenge to the
852 aerosol modelling community. The reanalysis does not perform as well with respect to mean bias and
853 RMSE over East Asia, Indian subcontinent, insular and peninsular Southeast Asia, where complicated
854 aerosol environments often exist. For example, dust is often mixed with various kinds of pollutants over
855 East Asia and the Indian subcontinent, which hinders satellite AOT retrievals and impacts model
856 performance through AOT data assimilation. Over insular Southeast Asia, constant high cloud cover
857 poses significant observability issues (Reid et al., 2013), reducing the availability of successful satellite
858 retrievals of AOT, in addition to artificial high AOTs caused by cirrus contamination in AERONET data.
859 This region also has a complicated fire regime that is systematically undersampled by the observations
860 used to drive the smoke emissions in the model (Miettinen et al., 2013). The large discrepancies
861 between the reanalysis and AERONET for coarse AOTs over insular and peninsular Southeast Asia affect
862 the reanalysis means and medians for total AOTs, but to a lesser degree, since fine mode aerosols are
863 the dominant aerosol type for the these regions. Most regions have r^2 between 0.5 and 0.8. W. CONUS

has the smallest r^2, which is about 0.376, among all regions, reflecting the challenge for the model to simulate the small variance of the AOT there.

3.2.3 Site-by-site validation

Site-by-site validation of the NAAPS reanalysis was conducted relative to the International Cooperative for Aerosol Prediction (ICAP) Multi Model Ensemble (ICAP-MME, Sessions et al., 2015) as a baseline. Overall, ICAP-MME was shown to outperform any individual models with regard to RMSE in 550 nm AOT forecast (Sessions et al., 2015). By ranking, the ICAP-MME was typically first or second against all models at individual sites using one-year worth of data. Since most of the ICAP models include AOT assimilation as well, the NAAPS reanalysis was compared to the ICAP-MME. The twenty-one AERONET sites used in the ICAP-MME study were agreed upon by the world's major center developers, as the most representative of each region. The same two seasonal periods (DJFMAM and JJASON of 2012) are used. In Fig. 4, these sites are marked with red squares. The ICAP-MME is run daily at 00 UTC for 6-hourly forecasts out to 120 hr. The best available ICAP MME data (closest to analysis) for this comparison is the consensus mean of 6-hr forecast at 00 UTC; thus, the NAAPS reanalysis is at an advantage in this comparison due to the lagged AOT assimilation cycle in the ICAP-MME.

Table 2 shows the name of each site, its location and the prevailing aerosol type, along with all statistics relating to the total AOT at 550 nm for the two seasons. The same statistics for fine and coarse mode AOTs are listed in Tables 3 and 4, respectively. The values of bias and RMSE are in bold, bold with underline, and italic, depending on whether the reanalysis performance is the same, better, or worse than the ICAP MME mean 6-hr forecast, respectively. Over a majority of the sites, the total AOT of the reanalysis is the same or better than the ICAP-MME with respect to bias and RMSE. The exceptions are the Beijing and Solar Village AERONET sites. Singapore is uncertain, as the low biases in fine mode AOT contributes less than half of the total low bias, implying the dominant bias is the coarse mode AOT bias,

887 which is affected by thin cloud contamination in AERONET data. Cases, where the reanalysis is the same
888 or better than the ICAP-MME in bias and RMSE occur less for the coarse-mode AOT than for the total
889 AOT. On the one hand, the total AOT is assimilated in the reanalysis while the coarse mode AOT is not.
890 So, the total AOT is better constrained with satellite observations. On the other hand, the ICAP-MME
891 consensus mean for dust/coarse mode AOT includes an additional independent aerosol model relative
892 to the total AOT consensus (five vs. four models), which makes the dust AOT ensemble exhibit better
893 performance among all the models compared with the total AOT ensemble performance (Sessions et al.,
894 2015).

895 The AOT seasonal difference is very clear for sites with outstanding seasonal aerosol features.
896 For example, higher total and fine AOT values attributed to biomass burning are observed in JJASON
897 over Alta Floresta, Rio Branco, and Singapore and in DJFMAM over Chiang Mai. Seasonal differences are
898 also found over Ilorin with higher AOT in DJFMAM relative to JJASON, due to both dust and biomass
899 burning activities. It is generally true that absolute bias and RMSE increase with increasing values of
900 AOT, so a seasonal variation in bias and RMSE is also discernable for the sites with large seasonal AOT
901 variations. r^2 of the above sites in their biomass burning seasons are generally very good (above 0.8
902 except for Singapore), indicating that the reanalysis captures the timing and variability of large smoke
903 episodes quite well.

904 Overall, the sign of the bias and the order of magnitude of the bias and RMSE values for the
905 selected sites are consistent with the regional evaluations in Fig. 10-12 (and the supplemental tables).
906 For high AOT sites (e.g., Banizoumbou, Beijing, Chiang Mai, Gandhi College, Ilorin and Kanpur), the
907 reanalysis generally has a low bias, as a result of the model and/or the data assimilation system being
908 incapable of capturing the amplitude of high AOT events. An exception is Solar Village, though its
909 dominant aerosol species, which is dust/coarse mode aerosol, is also biased low in AOT during DJFMAM.

910 Low bias in high AOT events is quite common among aerosols models (Kinne et al., 2006; Sessions et al.,
911 2015). The discrepancy can arise solely as a function of spatial and temporal resolution: the average AOT
912 for a grid cell in an aerosol plume will be systematically lower than the peak observed point AOT in that
913 plume. However, shortcomings of aerosol sources or insufficient representation of near-source aerosol
914 processes can also cause bias. Sometimes the discrepancy can be reduced by AOT assimilation, but the
915 probability of a successful retrieval declines for higher AOT events, and this phenomenon is amplified by
916 the application of AOT QA/QC procedures. The largest departure for both seasons in total AOT occurs
917 over Beijing, where the coarse mode bias contributes a little more to the total bias in DJFMAM and the
918 fine mode bias contributes a little more in JJASON. Among all sites, the maximum RMSE occurs over
919 Beijing in both seasons for the total and the fine mode AOT and in DJFMAM for coarse mode AOT.
920 JJASON RMSE is smaller for the reanalysis than for the ICAP-MME, implying that global models uniformly
921 don't do well here. Correlation coefficient r^2 of the coarse mode AOT at Beijing is also the worst for both
922 seasons, while r^2 values for the fine and total AOTs are reasonable (0.54 in DJFMAM and 0.76 in JJASON
923 for total AOT, and a little better for fine AOT). The frequent mixture of pollution, dust, and clouds, along
924 with varying surface properties also hinders satellite retrievals, not only reducing the number of
925 successful retrievals but also contributing to large errors in retrieved AOT (e.g, Shi et al., 2011b; Zhang et
926 al., 2014). Similar situations exist for Ilorin, where Sahelian biomass burning system is often mixed with
927 dust episodes in DJFMAM, and for Gandhi College and Kanpur, the two Indian sites, in both seasons.

928 For moderate to low AOT sites, including Cart Site, Chapais, GSFC, Minsk, Moldova, Monterey
929 and Palma de Mallorca, the reanalysis performs well, with the biases falling between -0.02 and 0.02,
930 RMSE values less than half of their site mean AOTs for all modes (all less than 0.07), and r^2 between
931 0.42 and 0.85. Over Crozet Island, a remote oceanic site in the Southern Indian Ocean, the reanalysis has
932 a relative large high bias (compared to its very low mean) likely due to overestimation of sea salt. On the

933 contrary, the fine mode AOT has a slight low bias, which may be an indication of insufficient DMS
934 emission or too much removal.

935 Several sites are affected by similar aerosol sources at different distances, allowing us to
936 examine transport phenomena using these sites. Banizoumbou, which is located deep in the Sahara, has
937 the largest bias (negative) and RMSE, and the lowest r^2 for the coarse and total AOT modes among all
938 the African-dust-impacted sites. Capo Verde, located on an island off the west coast of North Africa, has
939 high coarse mode AOT, but with much smaller bias and RMSE and high correlation (r^2 is ~0.88 for
940 DJFMAM and ~0.77 for JJASON for both total and coarse AOTs), benefiting from AOT assimilation.
941 Farther downwind of north Africa and across the Atlantic Ocean, Ragged Point in Barbados, shows even
942 smaller biases and RMSEs and very high correlation (r^2 greater than 0.81 for total AOT in both season,
943 and for coarse AOT in JJASON). Palma de Mallorca, which is a receptor site for Saharan dust transported
944 across the Mediterrean Sea, has bias, RMSE and correlation similar to Ragged Point.

945 The performance of the reanalysis has a tendency to increase with the distance from the source
946 region, especially over water. The main reasons for this are 1) aerosol models normally have larger
947 uncertainties in aerosol sources than aerosol transports (Kinne et al., 2003), 2) there is limited satellite
948 AOT data over the bright desert regions for the model to assimilate (Fig. 2), while there are a lot more
949 opportunities for the model AOT to be corrected by assimilation along dust transport paths, and 3) the
950 atmosphere acts to smooth out near-source variability that is often at finer scales than the effective
951 resolution of the model. These effects can also be seen when comparing the reanalysis performance
952 over Beijing and Baengyueong, an island site in South Korea downwind of Beijing, for both fine and
953 coarse mode AOTs.

954 3.3 AOT trend

There is debate over the use of AOT renanalyses to document and understand climatic trends, similar to the debate associated with meteorological reanalysis. However, the decadal trends derived from the reanalysis are largely in line with other studies using stand-alone satellite products (Zhang and Reid, 2010; Hsu et al., 2012) for a similar time period. This helps to evaluate the reanalysis from another perspective. Figure 13 shows the trend of the deseasonalized total AOT over the whole reanalysis period (2003-2013), using the same calculation method as in Zhang and Reid (2010), where the significance of the trend analysis is estimated following the method of Weatherhead et al. (1998). Many areas show trends consistent with the satellite-only results of Zhang and Reid (2010) and Hsu et al. (2012): Indian Bay of Bengal, Arabian Peninsula and Arabian Sea, Bohai Sea in East Asia and the downwind region of South African biomass burning area, which have a positive trend, and the east coast of North America, Europe, central South America biomass burning area and Southern Indian Ocean, which have a negative trend. The reanalysis also exhibits a weak negative trend off the coast of dusty West Africa that is similar to other studies, though not statistically significant. The non-trend (zero trend) region with statistical significance in the south subtropical Pacific Ocean is also consistent with other studies.

An arguable trend appears in the Maritime Continent, where Zhang and Reid (2010) report a non-significant positive trend while Hsu et al. (2012) and our reanalysis here report a non-significant or significant negative trend based on slightly different study periods (Study periods are 2000-2010, 1998-2010, and 2003-2013 in Zhang and Reid, Hsu et al. and this paper, respectively). Because 1997-1998 was a strong El Nino period and 2010-2012 are La Nina years, corresponding to strong and weak fire activities in the Maritime Continent, respectively, trends for these different periods can be expected to differ systematically. Studies show that the climate and the associated fire/smoke activity in the Maritime Continent are controlled by ENSO on the inter-annual time scale (e.g., Reid et al., 2012; van der Werf et al., 2004). The Maritime Continent is anomalously dry during El Nino years and experiences more fire activity and thus smoke aerosols compared to La Nina years, and there is a good correlation

between ENSO and AOT there (e.g., Hsu et al., 2012; Xian et al., 2013). The different AOT trends over the maritime continents obtained with the use of slightly different time periods suggest the importance of checking the possible controlling climate variability on aerosol trend analysis depending on the time scales of interest. Similarly, the negative AOT trend in north Africa and off the coast of West Africa is likely impacted by the Atlantic Multidecadal Oscillation (AMO), North Atlantic Oscillation (NAO) and ENSO activities as Saharan dust is also shown to be correlated with these climate variabilities (Evan et al., 2006; Hsu et al., 2012; Wang et al., 2012).

This reanalysis uses non-trending source functions for sulfate, DMS, organic aerosol emissions and dust erodibility. It is worth noting that even with static source functions and no volcanic source, the data assimilation has successfully picked up the positive trend downwind of the Hawaiian Islands due to the enhanced degassing activity of the Kilauea volcano since 2008 (e.g. Beirle et al., 2014). In a parallel model run, where AOT data assimilation is turned off, trends disappear over the east coast of North America and Europe or change sign over the Bay of Bengal while retaining their signs in most other regions (not shown). This indicates that AOT trends over the eastern US, Europe and Bay of Bengal are related to anthropogenic emission changes. Opposite to the trend shown in the DA run, West African and the downwind subtropical Atlantic region show a strong positive trend in the natural run. There could be many possible reasons, such as an artifact of stronger surface wind in the meteorological model over the study period, or changes in vegetation which are not captured in the meteorological model or the dust source function.

The positive trend over the Southern African biomass burning area and its downwind subtropical Atlantic region and the negative trend over central South America biomass burning region are by and large a result of increasing fire emissions over Southern Africa and decreasing fire emissions over South America exhibited in FLAMBE (not shown). The smoke emission trends in the above regions

1002 are consistent with the trends found with other satellite fire detection products for the same time
1003 period (Giglio et al., 2013). Trends over other regions are most likely relevant to climate variability or
1004 changes in climate, especially changes in meteorological variables that covary with aerosol processes.
1005 For example, the aforementioned negative trend over the Maritime Continent is very likely closely
1006 related to ENSO cycles. In another example, the decreasing dust trend in the North Africa dust outflow
1007 region of the tropical Atlantic is shown to be caused mainly by a reduction in surface winds over dust
1008 source regions rather than changes in land surface properties in modeling studies (Chin et al., 2014;
1009 Ridley et al., 2014).

1010 The Arabian Peninsula experiences increasing AOT, which may result from the observed
1011 decreasing precipitation for the similar time period (Almazroui et al., 2012). The negative AOT trend
1012 over the Southern Indian Ocean is consistent with the trend analysis using MISR AOT data (Murphy,
1013 2013). However, this trend in our analysis results solely from trends in the source and sink function,
1014 because AOT is not assimilated in this region in our system. The decreasing trend in the southern Indian
1015 Ocean AOT in the model is mainly caused by a decreasing trend in the surface winds in the
1016 meteorological model, NOGAPS (not shown). Observational studies, however, have found that wind
1017 speed over the southern oceans has increased in the past two decades (Young et al., 2011; Hande et al.,
1018 2012). The question of why the surface wind in NOGAPS decreases and AOT decreases in the southern
1019 oceans during the 2003-2013 time period requires additional investigation but beyond the scope of this
1020 study.

1021 Figure 14 shows the monthly mean NAAPS reanalysis and AERONET L2 modal AOT at six AERONET
1022 sites chosen for their relatively long-term record under different aerosol regimes: Alta Floresta in the
1023 Amazon, dominated by biomass burning smoke during the burning season; Beijing in East Asia,
1024 dominated by anthropogenic fine mode aerosols year round with mixed dust and pollutions in the spring

time; Capo Verde off the west coast of North Africa, dominated by Sahara/Sahel dust, GSFC in east CONUS, dominated by anthropogenic fine mode aerosols, Solar Village in the Arabian Peninsula, dominated by dust, and Venise in Italy, dominated by pollution-related fine mode aerosols and influenced by Saharan dust in spring time. Also shown are linear regression lines based on the total AOTs, indicative of AOT trends. Annotations in each time series show bias, RMSE and r^2 of the total AOT and the dominant modal AOT, calculated with reanalysis monthly averages (unpaired). Statistics from a paired comparison using reanalysis data sampled to match available AERONET data are shown in parentheses.

Overall, the reanalysis follows the seasonal and interannual variability in AERONET data for the total AOT quite well, and to a lesser extent for the coarse and fine mode AOTs. The pairwise comparison shows better correlation with AERONET than that calculated with all data, and, generally smaller absolute bias and RMSE. The decreasing trends over Alta Floresta, GSFC and Venise, the increasing trend over Beijing (slight) and Solar Village, and the insignificant trend over Capo Verde are consistent with the regional trends shown in Fig. 13, and qualitatively agree with AERONET. Over GSFC, the reanalysis captures the evident decrease in total and fine mode AOT since 2008. The June-July-August average AOT drops about 0.14 (from 0.37 to 0.23) for the total AOT and 0.12 (from 0.29 to 0.17) for the fine mode AOT comparing the years before and after 2008. It drops about 0.09 (from 0.31 to 0.22) for the total AOT and 0.08 (from 0.27 to 0.19) for the fine mode AOT in the reanalysis, with a low bias in total AOT and a minimal bias in fine mode AOT for the season.

4 Summary and discussion

This paper describes a near 11-year global 550 nm modal AOT reanalysis product developed at the Naval Research Laboratory, with a spatial resolution of 1x1 degree and a temporal resolution of 6 hours. The reanalysis uses the Navy Aerosol Analysis and Prediction System (NAAPS) with regionally-tuned

source functions at its core and assimilates quality-controlled Terra and Aqua Collection 5 Moderate Resolution Imaging Spectroradiometer (MODIS) and Multi-angle Imaging SpectroRadiometer (MISR) AOT. Aerosol wet deposition in the tropics is constrained with satellite retrieved precipitation. Dry deposition parameters over ocean are also adjusted by minimizing AOT corrections in AOT assimilation. By validating the reanalysis fine and coarse mode AOTs and total AOT with Aerosol Robotic Network (AERONET) Level-2 product, we report the following findings:

4.1 Global representation: Compared with 6-hr-average AERONET data, global mean RSME values for both fine and coarse mode AOTs are around 0.1, and the RMSE for the total AOT is ~ 0.14. AOT RMSE decreases 50% when monthly averaging is applied. On a global average, coarse-mode AOT has a slight negative bias (-0.02) which is partially compensated by a slight positive bias of the fine mode AOT (0.01). In general, the fine mode AOT matches AERONET slightly better than the coarse mode AOT, reflected in the bias, RMSE and correlation. These numbers vary among different regions presumably because of regionally specific aerosol features.

Since total AOT is being assimilated, the total AOT has a smaller uncertainty relative to the coarse and fine mode AOT. Currently, there is no way to validate speciated AOTs if two or more aerosol species are present in the same size mode. We would expect the relative uncertainty of the speciated AOTs to be larger than the modal AOTs. The data quality of satellite-retrieved AOT is generally better over water than over land because of the relatively simple surface optical properties of water (e.g., Levy et al., 2005, Remer et al., 2005). Under the same AOT data assimilation frequency (or same amount of data to be assimilated), the reanalysis performs relatively better over oceanic and coastal regions/sites than land regions/sites.

4.2 Regional representation: The reanalysis captures the regional and seasonal AOT variations skillfully. The range of the regional reanalysis AOT values are generally smaller than those of AERONET (i.e., high bias for small AOTs and low bias for high AOTs), which is commonly seen among aerosol models,

especially with coarse spatial and temporal resolution (e.g., Kinne et al., 2006; Sessions et al., 2015). Challenging regions for the reanalysis are East Asia, Indian subcontinent and Sahel, where there are often mixed fine and coarse mode aerosols. The reanalysis generally performs better in the long-range transport regions than the source regions. For example, the reanalysis AOT of the Caribbean islands sites, which are the receptor sites of African dust, matches AERONET observations better than the land sites within the African continent. A field campaign analysis of remotely transported smoke aerosols from Borneo and Sumatra islands found good agreement between the reanalysis AOT and the smoke concentrations therein and in-situ measurements taken in the open ocean west of the Philippines (Reid et al., 2014).

4.3 Trends: The trends calculated from the reanalysis are similar to other studies using standalone satellite products (Zhang and Reid, 2010; Hsu et al., 2012) in both aerosol transport regions and source regions. Over regionally representative sites, the reanalysis trend in modal AOT also agrees qualitatively well with the trend in AERONET data. This provides a reassurance of the quality of the reanalysis product. It is also worth noting that without trending source functions for sulfate and organic aerosols precursors, the data assimilation system has successfully reproduced regional AOT trends that are related to emission changes in the past decade. For example, a positive trend over India is attributed to emission growth. Signals of other low-frequency climate variability are also discernable in the reanalysis AOT. For example, using an earlier version of the NAAPS AOT analysis, the modulation effect of the Madden-Julian Oscillation on smoke AOT over the Maritime Continent is found (Reid et al., 2012).

4.4 Role of AOT data assimilation: Overall, the data assimilation system is very effective in correcting the modeled AOT and bringing it as close as possible to the satellite observations, and spreading the information to the neighboring grid cells through a correlation length scale. In the time steps following assimilation, the information is further propagated downstream. The data assimilation

system plays an indispensable role in picking up AOT trends in the regions affected by emission changes that are not represented in the model. However, the data assimilation system, associated with the assimilatable data, also has limitations. Satellite AOT retrievals characterize the optical properties of a column, and it does not carry any information about aerosol vertical profiles or speciation. So the total AOT is constrained through AOT data assimilation. The relative vertical profile in 3-D extinction and speciation of the aerosols are uniformly varied to match the posterior AOT. The geographical coverage of the MODIS+MISR data to be assimilated can cover only up to about a quarter of the Earth in one data assimilation cycle (Fig. 1). AOT of one area can be updated by the data assimilation system only once per day on average (at most twice per day) and only during the local daytime. This affects the aerosol diurnal cycle in the reanalysis, as all the nighttime AOT are purely driven by the natural model while daytime AOT can be controlled by the data assimilation system. Repetitively adding or shedding aerosol mass and thus AOT in one area through data assimilation can make the AOT evolution unphysical. Because AERONET measurements occur during the local daytime, the validation results here may not represent the reanalysis skill for other times of day.

4.5 *Data consistency in time*: Even though the data assimilation system has the capability of capturing the trend observed in stand-alone satellite or AERONET AOT analyses, the inconsistency in the meteorological analysis of Navy Operational Global Atmospheric Prediction System (NOGAPS) in the past decade poses a big challenge in the development of a long term global AOT reanalysis product. NOGAPS experienced several upgrades in the reanalysis period, including improved land surface parameterization, which impacts dust production trends.

A meteorological reanalysis is intended to provide a more consistent atmospheric state for aerosol simulations. But meteorological reanalyses have a data consistency issue as well, because observations being assimilated change significantly with time (e.g., Dee et al., 2011). For example,

with the ever-increasing satellite observations of the past two decades, more and more satellite data are being assimilated for one or more meteorological variables. With the demise or periodic malfunction of some satellite instruments, some data became unavailable. This impacts the final meteorological reanalysis, and consequently the AOT reanalysis. The NOAA Climate Prediction Center MORPHing (CMORPH) precipitation data, which is used to replace NOGAPS precipitation in the Tropics, is only available after December 2002. Its usage can impact regional AOT significantly in a natural model run (Xian et al., 2009). For areas not covered by the CMORPH product, any model precipitation performance change in time can be a potential issue for AOT trend analysis.

4.6 Recommendations for application

a) It is ideal for quick and consistent identification of large aerosol events globally or regionally. It can serve as a reference and provide the general background aerosol information without temporal or spatial discontinuity for field campaign analysis.
b) The reanalysis AOT can be used to provide global and regional AOT climatologies for climate and applied science applications.
c) The reanalysis AOT can be used in different scale analysis, from daily to inter-annual. The diurnal AOT analysis should be performed with caution considering the possible artifact feature introduced by the AOT assimilation cycle.

Our future direction for the NAAPS aerosol reanalysis will be focused on 3-D extinction and mass concentration of single aerosol species, with special emphasis on the vertical dimension. The ability of NAAPS assimilating the Cloud-Aerosol Lidar with Orthogonal Polarization (CALIOP) lidar backscatter coefficient data (Campbell et al., 2010; Zhang et al., 2011, 2014) will aid in this effort.

Code and data availability:

The NAAPS model code is a property of the U.S. Naval Research Laboratory and is not available to the public. However, the NAAPS reanalysis data is available at http://usgodae.org/cgi-bin/datalist.pl?dset=nrl_naaps_reanalysis&summary=Go . The data on this server are updated as model improvements are made and reruns are completed.

Acknowledgement:

The development of the NAAPS reanalysis was an outcome of the needs of multiple projects, and largely supported by the Office of Naval Research Code 322 and the NASA Interdisciplinary Science Program. Additional support was provided by the NRL Base Program and the Office of Naval Research 35. The development team is grateful to the effort of the operational NASA-MODIS and MISR aerosol teams for the development and implementation of their level two products. We are likewise grateful to the NASA land team for the development of their fire products. The NASA Aerosol Robotic Network (AERONET) data is key to verifying models such as the NAAPS reanalysis and the use of this federated network's data is gratefully acknowledged.

References:

Ahmadov R., McKeen S.A., Robinson A.L., Bahreini R., Middlebrook A., deGouw J., Meagher J., Hsie E.-Y., Edgerton E., Shaw S., Trainer M.: A volatility basis set model for summertime secondary organic aerosols over the eastern U.S. in 2006. J. Geophys. Res.,117, D06301, doi:10.1029/2011JD016831, 2012.

Almazroui, M., Nazrul Islam, M., Athar, H., Jones, P. D. and Rahman, M. A.: Recent climate change in the Arabian Peninsula: annual rainfall and temperature analysis of Saudi Arabia for 1978–2009. Int. J. Climatol., 32, 953–966, 2012.

Antoine, D., and Nobileau, D.: Recent increase of Saharan dust transport over the Mediterranean Sea, as revealed from ocean color satellite (SeaWiFS) observations, J. Geophys. Res., 111, D12214, doi:10.1029/2005JD006795, 2006.

Bathe, K.J. : Finite Element Procedures. Cambridge, MA: Klaus-Jürgen Bathe. ISBN 097900490X, 2006.

Beirle, S., Hörmann, C., Penning de Vries, M., Dörner, S., Kern, C., and Wagner, T.: Estimating the volcanic emission rate and atmospheric lifetime of SO_2 from space: a case study for Kīlauea volcano, Hawai`i, Atmos. Chem. Phys., 14, 8309-8322, 2014.

Benedetti, A., Morcrette, J.-J., Boucher, O., Dethof, A., Engelen, R. J., Fisher, M., Flentje, H., Huneeus, N., Jones, L., Kaiser, J. W., Kinne, S., Mangold, A., Razinger, M., Simmons, A. J., and Suttie, M.: Aerosol analysis and recast in the European centre for Medium-RangeWeather Forecasts Integrated Forecast System: 2. Data assimilation, J. Geophys. Res., 114, D13205, doi:10.1029/2008JD011115, 2009.

Benkovitz, C. M., T. Scholtz, L. Pacyna, L. Tarrson, J. Dignon, E. Voldner, P. A. Spiro, and T. E. Graedel : Global gridded inventories of anthropogenic emissions of sulphur and nitrogen. J. Geophys. Res., 101, 29239-29253, 1996.

Bond, T. C., D. G. Streets, K. F. Yarber, S. M. Nelson, J.-H. Woo, and Z. Klimont, A technology-based global inventory of black and organic carbon emissions from combustion, J. Geophys. Res., 109, D14203, doi:10.1029/2003JD003697, 2004.

Bond, T. C., et al.: Bounding the role of black carbon in the climate system: A scientific assessment, J. Geophys. Res. Atmos., 118, 5380–5552, 2013.

Buchard, V., da Silva, A. M., Colarco, P. R., Darmenov, A., Randles, C. A., Govindaraju, R., Torres, O., Campbell, J., and Spurr, R.: Using the OMI aerosol index and absorption aerosol optical depth to evaluate the NASA MERRA Aerosol Reanalysis, Atmos. Chem. Phys., 15, 5743-5760, 2015.

Campbell, J. R., J. S. Reid, D. L. Westphal, J. Zhang, E. J. Hyer, and E. J. Welton: CALIOP aerosol subset processing for global aerosol transport model data assimilation, J of Sel. Topics in Appl. Earth Obs. and Rem. Sens., 3, 203-214, 2010.

Campbell, J. R., Reid, J. S., Westphal, D. L., Zhang, J., Tackett, L., Chew B. N., Welton, E. J., Shimizu, A., Sugimoto, N. , Aoki, K., Winker, D. M. , Characterizing the vertical profile of aerosol particle extinction and linear depolarization over Southeast Asia and the Maritime Continent: The 2007–2009 view from CALIOP, Atmos. Res., 122, 520-543, 2013.

Chew, B. N., J. R. Campbell, J. S. Reid, D. M. Giles, E. J. Welton, S. V. Salinas and S. C. Liew: Tropical cirrus cloud contamination in sun photometer data, Atmos. Environ., Atmos. Environ., 45, 6724-6731, 2011.

Chin, M, Diehl T, Tan Q, Prospero J, Kahn R, Remer L, Yu H, Sayer A, Bian H, Geogdzhayev I, Holben B, Howell S, Huebert B, Hsu N, Kim D, Kucsera T, Levy R, Mishchenko M, Pan X, Quinn P, Schuster G, Streets D, Strode S, Torres O, Zhao X.: Multi-decadal aerosol variations from 1980 to 2009: a perspective from observations and a global model. Atmos. Chem. Phys. 14, 3657-3690, 2014.

Christensen, J. H. :The Danish eulerian hemispheric model—A three dimensional air pollution model used for the Arctic, Atmos. Environ., 31, 4169-4191, 1997.

Colarco, P., A. da Silva, M. Chin, and T. Diehl: Online simulations of global aerosol distributions in the NASA GEOS-4 model and comparisons to satellite and ground-based aerosol optical depth, J. Geophys. Res., 115, D14207, doi:10.1029/2009JD012820, 2010.

Collins, W. D., P. J. Rasch, B. E. Eaton, B. V. Khattatov, J.-F. Lamarque, and C. S. Zender: Simulating aerosols using a chemical transport model with assimilation of satellite aerosol retrievals: Methodology for INDOEX, J. Geophys. Res., 106, 7313–7336, 2001.

Dai, A.: Precipitation characteristics in eighteen coupled climate models, J. Climate, 19, 4605-4630, 2006.

Daley, R. and Barker, E.: NAVDAS: Formulation and diagnostics, Mon. Weather Rev., 129, 869-883, 2001.

Dee, D. P., Uppala, S. M., Simmons, A. J., Berrisford, P., Poli, P., Kobayashi, S., Andrae, U., Balmaseda, M. A., Balsamo, G., Bauer, P., Bechtold, P., Beljaars, A. C. M., van de Berg, L., Bidlot, J., Bormann, N., Delsol, C., Dragani, R., Fuentes, M., Geer, A. J., Haimberger, L., Healy, S. B., Hersbach, H., Hólm, E. V., Isaksen, L., Kållberg, P., Köhler, M., Matricardi, M., McNally, A. P., Monge-Sanz, B. M., Morcrette, J.-J., Park, B.-K., Peubey, C., de Rosnay, P., Tavolato, C., Thépaut, J.-N. and Vitart, F. : The ERA-Interim reanalysis: configuration and performance of the data assimilation system. Q.J.R. Meteorol. Soc., 137, 553–597, 2011.

Diehl, T., Heil, A., Chin, M., Pan, X., Streets, D., Schultz, M., and Kinne, S.: Anthropogenic, biomass burning, and volcanic emissions of black carbon, organic carbon, and SO2 from 1980 to 2010 for hindcast model experiments, Atmos. Chem. Phys. Disc. 12 : 24895-24954, 2012.

Donahue, N. M., A. L. Robinson, C. O. Stanier, and S. N. Pandis: Coupled partitioning, dilution, and chemical aging of semivolatile organics. Environ. Sci. Technol. 40, 2635 – 2643, 2006.

Dubovik, O., Holben, B., Eck, T. F., Smirnov, A., Kaufman, Y. J., King, M. D., Tanré, D. and Slutsker, I.: Variability of Absorption and Optical Properties of Key Aerosol Types Observed in Worldwide Locations. J. Atmos. Sci., 59, 590–608, 2002.

Evan, A. T., A. K. Heidinger, and P. Knippertz: Analysis of winter dust activity off the coast of West Africa using a new 24-year over-water advanced very high resolution radiometer satellite dust climatology, J. Geophys. Res., 111, D12210, doi:10.1029/2005JD006336, 2006.

Fromm, M. D., and R. Servranckx: Transport of forest fire smoke above the tropopause by supercell

convection, Geophys. Res. Lett., 30(10), 1542, doi:10.1029/2002GL016820, 2003.
Giglio, L., J. T. Randerson, and G. R. van der Werf: Analysis of daily, monthly, and annual burned area using the fourth-generation global fire emissions database (GFED4), J. Geophys. Res. Biogeosci., 118, doi:10.1002/jgrg.20042, 2013.
Ginoux, Paul, M Chin, I Tegen, J M Prospero, B Holben, O Dubovik, and Shian-Jiann Lin: Sources and distributions of dust aerosols simulated with the GOCART model. J. Geophys. Res., 106(D17), 20255-20273, 2001.
Gordon, H. R. : Atmospheric correction of ocean color imagery in the Earth Observing System era, J. Geophys. Res., 102(D14), 17081–17106, 1997.
Granier, Claire et al., Evolution of anthropogenic and biomass burning emissions of air pollutants at global and regional scales during the 1980–2010 period, Climate Change 109 (1-2): 163-190, 2011.
Hande, L. B., S. T. Siems, and M. J. Manton: Observed Trends in Wind Speed over the Southern Ocean, Geophys. Res. Lett., 39, L11802, doi:10.1029/2012GL051734, 2012.
Hänel, G.: The properties of atmospheric aerosol particles as functions of relative humidity at thermodynamic equilibrium with surrounding moist air, Geophy., 19, 73-188., 1976.
Heald, C. L., D. J. Jacob, P. I. Palmer, M. J. Evans, G. W. Sachse, H. B. Singh, and D. R. Blake, Biomass burning emission inventory with daily resolution: Application to aircraft observations of Asian outflow, J. Geophys. Res., 108(D21), 8811, doi:10.1029/2002JD003082, 2003.
Hegg, D. A., D. S. Covert, K. Crahan, and H. H. Jonsson, The dependence of aerosol light-scattering on RH over the Pacific Ocean, Geophys. Res. Lett., 29(8), doi:10.1029/2001GL014495, 2002.
Hertel, O., Christensen, J., Runge, E., Asman, W. A. H., Berkowicz, R., Hovmand, M. and Hov, O.: Development and testing of a new variable scale air pollution model-ACDEP. Atmos. Env., 29, 1267-1290, 1995.
Hess, M., P. Koepke, P., and Schult, I.: Optical Properties of Aerosols and Clouds: The Software Package OPAC. Bull. Amer. Meteor. Soc., 79, 831–844, 1998.
Hoffmann, M. R. and Calvert, J. G.: Chemical Transformation Modules for Eulerian Acid Deposition Models: Volume II, the Aqueous-phase Chemistry, U.S. Environmental Protection Agency, Research Triangle Park, NC. 1985.
Hogan, T. F. and L. Brody: Sensitivity Studies of the Navy's Global Forecast Model Parameterizations and Evaluation of Improvements to NOGAPS. Mon. Wea. Rev., 121, 2373-2395, 1993.
Hogan, T. F., Liu, M., Ridout, J. S., Peng, M. S., Whitcomb, T. R., Ruston, B. C., Reynolds, C. A., Eckermann S. D., Moskaitis, J. R., Baker, N. L., McCormack, J. P., Viner, K. C., McLay, J. G., Flatau, M. K., Xu, L., Chen, C., and Chang, S. W.,: The Navy Global Environmental Model. Oceanography, Special Issue on Navy Operational Models, 27, No. 3. 2014.
Hogan, T.F. and T.E. Rosmond: The description of the Navy Operational Global Atmospheric Prediction System's spectral forecast model. Mon. Wea. Rev., 119, 1786-1815, 1991.
Holben, B. N., Eck, T. F., Slutsker, I., Tanre, D., Buis, J. P., Setzer, A., Vermote, E., Reagan, J. A., Kaufman, Y. J., Nakajima, T., Lavenu, F., Jankowiak, I., and Smirnov, A.: AERONET - A federated instrument network and data archive for aerosol characterization, Remote Sens. Environ., 66, 1-16, 1998.
Holben, B. N., Tanré, D., Smirnov, A., Eck, T. F., Slutsker, I., Abuhassan, N., Newcomb, W. W., Schafer, J. S., Chatenet, B., Lavenu, F., Kaufman, Y. J., Castle, J. V., Setzer, A., Markham, B., Clark, D., Frouin, R., Halthore, R., Karneli, A., O'Neill, N. T., Pietras, C., Pinker, R. T., Voss, K., and Zibordi, G.: An emerging ground-based aerosol climatology: Aerosol optical depth from AERONET, J. Geophys. Res.-Atmos., 106, 12067-12097, 2001.
Houweling, S., W. Hartmann, I. Aben, H. Schrijver, J. Skidmore, G.-J. Roelofs, and F.-M. Breon: Evidence of systematic errors in SCIAMACHY-observed CO_2 due to aerosols, Atmos. Chem. Phys., 5, 3003–3013, 2005.
Hsu, N. C., Gautam R, Sayer A, Bettenhausen C, Li C, Jeong M, Tsay S, Holben B. Global and regional

trends of aerosol optical depth over land and ocean using SeaWiFS measurements from 1997 to 2010. Atmos. Chem. Phys. 12, 8037-8053, 2012.
Hsu, N. C., Tsay, S.-C., King, M. D., and Herman, J. R.: Aerosol properties over bright-reflecting source regions, IEEE T. Geosci. Remote Sens., 42, 557–569, 2004.
Huang, J., N. C. Hsu, S.-C. Tsay, M.-J. Jeong, B. N. Holben, T. A. Berkoff, and E. J. Welton: Susceptibility of aerosol optical thickness retrievals to thin cirrus contamination during the BASE-ASIA campaign, J. Geophys. Res., 116, D08214, doi:10.1029/2010JD014910, 2011.
Hyer, E. J. , Reid, J. S., Prins, E. M., Hoffman, J. P., Schmidt, C. C., Miettinen, J. I., Giglio L., Patterns of fire activity over Indonesia and Malaysia from polar and geostationary satellite observations, Atmos. Res., 122, 504-519, 2013
Hyer, E. J., Reid, J. S., and Zhang, J.: An over-land aerosol optical depth data set for data assimilation by filtering, correction, and aggregation of MODIS Collection 5 optical depth retrievals, Atmos. Meas. Tech., 4, 379–408, 2011.
Inness, A., Baier, F., Benedetti, A., Bouarar, I., Chabrillat, S., Clark, H., Clerbaux, C., Coheur, P., Engelen, R. J., Errera, Q., Flemming, J., George, M., Granier, C., Hadji-Lazaro, J., Huijnen, V., Hurtmans, D., Jones, L., Kaiser, J. W., Kapsomenakis, J., Lefever, K., Leitão, J., Razinger, M., Richter, A., Schultz, M. G., Simmons, A. J., Suttie, M., Stein, O., Thépaut, J.-N., Thouret, V., Vrekoussis, M., Zerefos, C., and the MACC team: The MACC reanalysis: an 8 yr data set of atmospheric composition, Atmos. Chem. Phys., 13, 4073-4109, 2013.
IPCC: Climate Change 2007: The Physical Science Basis. Contribution of Working Group I to the Fourth Assessment Report of the Intergovernmental Panel on Climate Change [Solomon, S., D. Qin, M. Manning, Z. Chen, M. Marquis, K.B. Averyt, M.Tignor and H.L. Miller (eds.)]. Cambridge University , Press, Cambridge, United Kingdom and New York, NY, USA, 2007.
IPCC: Climate Change 2013: The Physical Science Basis. Contribution of Working Group I to the Fifth Assessment Report of the Intergovernmental Panel on Climate Change [Stocker, T.F., D. Qin, G.-K. Plattner, M. Tignor, S.K. Allen, J. Boschung, A. Nauels, Y. Xia, V. Bex and P.M. Midgley (eds.)].Cambridge University Press, Cambridge, United Kingdom and New York, NY, USA, 2013.
Iversen, T.: Numerical modeling of the long range atmospheric transport of sulphur dioxide and particulate sulphate to the arctic, Atmos. Env., 23, 2571–2595, 1989.
Janowiak, J.E., Kousky, V.E., Joyce, R.J.: Diurnal cycle of precipitation determined from the CMORPH high spatial and temporal resolution global precipitation analyses. J. Geophys. Res. 110, D23105, 2005.
Jeong, J. I., Park, R., Woo, J-H., Han Y-J. and Yi, S-M.: Source contributions to carbonaceous aerosol concentrations in Korea. Atmos. Environ., 45, 1116-1125, 2011.
Jimenez, J. L. et al.: Evolution of organic aerosols in the atmosphere. Science, 326, 1525-1529, 2009.
Joyce, R.J., Janowiak, J.E., Arkin, P.A., Xie, P.: CMORPH: a method that produces global precipitation estimates from passivemicrowave and infrared data at high spatial and temporal resolution. J. Hydromet. 5, 487–503, 2004.
Kahn, R. A., B. J. Gaitley, M. J. Garay, D. J. Diner, T. F. Eck, A. Smirnov, and B. N. Holben: Multiangle Imaging SpectroRadiometer global aerosol product assessment by comparison with the Aerosol Robotic Network, J. Geophys. Res., 115, D23209, doi:10.1029/2010JD014601, 2010.
Kahn, R. A., Nelson, D. L., Garay, M., Levy, R. C., Bull, M. A., Diner, D. J., Martonchik, J. V., Paradise, S. R., and Hansen, E. G., and Remer, L. A.: MISR Aerosol product attributes, and statistical comparisons with MODIS. IEEE Trans. Geosci. Remt. Sens, 47, 4095–4114, 2009.
Kahn, R. A., Y. Chen, D. L. Nelson, F.-Y. Leung, Q. Li, D. J. Diner, and J. A. Logan: Wildfire smoke injection heights: Two perspectives from space, Geophys. Res. Lett., 35, L04809, doi:10.1029/2007GL032165. 2008.
Kaku, K. C., J. S. Reid, N. T. O'Neill, P. K. Quinn, D. J. Coffman, and T. F. Eck: Verification and application

of the extended spectral deconvolution algorithm (SDA+) methodology to estimate aerosol fine and coarse mode extinction coefficients in the marine boundary layer, Atmos. Meas. Tech., 7, 3399-3412, 2014.

Kalnay, E., M. Kanamitsu, R. Kistler, W. Collins, D. Deaven, L. Gandin, M. Iredell, S. Saha, G. White, J. Woollen, Y. Zhu, A. Leetmaa, R. Reynolds, M. Chelliah, W. Ebisuzaki, W. Higgins, J. Janowiak, K. C. Mo, C. Ropelewski, J. Wang, R. Jenne, D. Joseph: The NCEP/NCAR 40-year reanalysis project, Bull. Amer. Meteor. Soc., 77, 437-470, 1996.

Kappos, A. D., Brickmann, P., Elkmann, T., et al.: Health effects of particles in the ambient air, Int. J. of Hygene and Environ. Health, 207, 399-407, 2004.

Kinne, S., et al.: An AeroCom initial assessment -- optical properties in aerosol component modules of global models. Atmos. Chem. Phys. 6, 1815-1834, 2006.

Kinne, S., et al., Monthly averages of aerosol properties: A global comparison among models, satellite data, and AERONET ground data, J. Geophys. Res., 108(D20), 4634, doi:10.1029/2001JD001253, 2003.

Laden, F., Neas, L. M., Dockery, D. W., and Schwartz, J.: Association of fine particulate matter from different sources with daily mortanlity in six US cities, Environ. Health Perspectives, 108, 941-947, 2000.

Lana, A., et al.: An updated climatology of surface dimethlysulfide concentrations and emission fluxes in the global ocean, Global Biogeochem. Cycles, 25, GB1004, doi:10.1029/2010GB003850. 2011.

Levy, R. C., Remer, L. A., Kleidman, R. G., Mattoo, S., Ichoku, C., Kahn, R., and Eck, T. F.: Global evaluation of the Collection 5 MODIS dark-target aerosol products over land, Atmos. Chem. Phys., 10, 10399–10420, 2010.

Levy, R. C, Remer, L. A, Mattoo, S, Vermote, EF, Kaufman, Y. J: Second-generation operational algorithm: Retrieval of aerosol properties over land from inversion of Moderate Resolution Imaging Spectroradiometer spectral reflectance. J. Geophys. Res-Atmos. 112, D13211, doi:10.1029/2006JD007811, 2007.

Levy, R. C., et al.: Evaluation of the MODIS aerosol retrievals over ocean and land during CLAMS, J. Atmos. Sci., 62(4), 974–992, 2005.

Li-Jones X, H. B. Maring, J. M. Prospero: Effect of relative humidity on light scattering by mineral dust aerosol as measured in the marine boundary layer over the tropical Atlantic Ocean, J. Geophys. Res. 103, 31113-31121, 1998.

Martonchik, J. V., R. A. Kahn, and D. J. Diner, “Retrieval of aerosol properties over land using MISR observations,” in Satellite Aerosol Remote Sensing Over Land, A. Kokhanovsky, Ed. Berlin, Germany: Springer-Verlag, 2009.

May, D. A., Stowe, L. L., Hawkins, J. D., McClain, E. P.; A correction for Saharan dust effects on satellite sea-surface temperature-measurements, J. Geophys. Res., 97, 3611-3619, 1992.

Miettinen, J., E. Hyer, A. S. Chia, L. K. Kwoh, and S. C. Liew: Detection of vegetation fires and burnt areas by remote sensing in insular Southeast Asian conditions: current status of knowledge and future challenges, Int. J. Remote Sens., 34(12), 4344-4366, 2013.

Miller, R.L., R.V. Cakmur, J.P. Perlwitz, I.V. Geogdzhayev, P. Ginoux, K.E. Kohfeld, D. Koch, C. Prigent, R. Ruedy, G.A. Schmidt, and I. Tegen: Mineral dust aerosols in the NASA Goddard Institute for Space Sciences ModelE atmospheric general circulation model. J. Geophys. Res., 111, D06208, doi:10.1029/2005JD005796, 2006.

Ming, Y, Russell L. M.: Predicted hygroscopic growth of sea salt aerosol. J. Geophys. Res.-Atmos., 106, 28259-28274, 2001.

Mishchenko, M. I., Geogdzhayev, I. V., Cairns, B., Rossow, W. B. and Lacis, A. A.: Aerosol retrievals over the ocean using channel 1 and 2 AVHRR data: A sensitivity analysis and preliminary results, Appl. Opt., 38, 7325–7341, doi:10.1364/AO.38.007325, 1999.

Monahan, E. C., D. E. Spiel, and K. L. Davidson: A model of marine aerosol generation via whitecaps and wave disruption, in Oceanic Whitecaps and Their Role in Air-Sea Exchange Processes, edited by E.C. Monahan and G. MacNiocaill, 167– 174, Springer, New York, 1986.

Morcrette, J.-J., Boucher, O., Jones, L., Salmond, D., Bechtold, P., Beljaars, A., Benedetti, A., Bonet, A., Kaiser, J. W., Razinger, M., Schulz, M., Serrar, S., Simmons, A. J., Sofiev, M., Suttie, M., Tompkins, A. M., and Untch, A.: Aerosol analysis and forecast in the European Centre for Medium-RangeWeather Forecasts Integrated Forecast System: Forward modeling, J. Geophys. Res., 114, D06206, doi:10.1029/2008JD011235, 2009.

Murphy, D. M.: Little net clear-sky radiative forcing from recent regional redistribution of aerosols, Nature Geoscience, 6, 258-262, 2013.

Obukhov, A.M : Turbulence in an atmosphere with a non-uniform temperature (English Translation). Boundary-Layer Meteorology 2: 7–29, 1971.

Olivier J., J. Peters, C. Granier, G. Petron, J.F. Muller and S. Wallens, Present and future surface emissions of atmospheric compounds , POET report #2, EU project EVK2-1999-00011, 2003.

O'Neill, N.T., T.F.Eck, B.N.Holben, A.Smirnov, O.Dubovik, and A.Royer: Bimodal size distribution influences on the variation of Angstrom derivatives in spectral and optical depth space, J. Geophys. Res., 106, 9787-9806, 2001.

O'Neill, N. T., Eck, T. F., Smirnov, A., Holben, B. N., and Thulasiraman S.: Spectral discrimination of coarse and fine mode optical depth. J. Geophys. Res., 108, D05212, doi:10.1029/2002JD002975, 2003.

Pankow, J. F., An absorption model of gas/particle partitioning of organic compounds in the atmosphere, Atmos. Environ., 28, 189-193, 1994.

Pérez, C., Haustein, K., Janjic, Z., Jorba, O., Huneeus, N., Baldasano, J. M., Black, T., Basart, S., Nickovic, S., Miller, R. L., Perlwitz, J. P., Schulz, M., and Thomson, M.: Atmospheric dust modeling from meso to global scales with the online NMMB/BSC-Dust model – Part 1: Model description, annual simulations and evaluation, Atmos. Chem. Phys., 11, 13001–13027, doi:10.5194/acp-11-13001-2011, 2011.

Reid, J. S., R. Koppmann, T. Eck, and D. Eleuterio: A review of biomass burning emissions part II: Intensive physical properties of biomass burning particles, Atmos. Chem. Phys., 5, 99–825, 2005a.

Reid, J. S., T. Eck, S. Christopher, O. Dubovik, R. Koppmann, D. Eleuterio, B. Holben, E. Reid, and J. Zhang: A review of biomass burning emissions part III: Intensive optical properties of biomass burning particles, Atmos. Chem. Phys., 5, 827–849, 2005b.

Reid, J. S., Hyer, E. J., Prins, E. M., Westphal, D. L., Zhang, J., Wang, J., Christopher, S. A., Curtis, C. A., Schmidt, C. C., Eleuterio, D. P., Richardson, K. A., and Hoffman, J. P.: Global Monitoring and Forecasting of Biomass-Burning Smoke: Description of and Lessons from the Fire Locating and Modeling of Burning Emissions (FLAMBE) Program, IEEE J. Sel. Top. Appl., 2, 144–162, JSTARS-2009-00034, 2009.

Reid, J. S., N. D. Lagrosas, H. H. Jonsson, E. A. Reid, W. R. Sessions, J. B. Simpas, S. N. Uy, T. J. Boyd, S. A. Atwood, D. R. Blake, J. R. Campbell, S. S. Cliff, B. N. Holben, R. E. Holz, E. J. Hyer, P. Lynch, S. Meinardi, D. J. Posselt, K. A. Richardson, S. V. Salinas, A. Smirnov, Q. Wang, L. E. Yu, and J. Zhang, Observations of the temporal variability in aerosol properties and their relationships to meteorology in the summer monsoonal South China Sea/East Sea: the role of monsoonal flows, the Madden–Julian Oscillation, tropical cyclones, squall lines and cold pools. Atmos. Chem. Phys. Discuss., 14, 20521-20584, 2014.

Reid, J. S., et al.: Observing and Understanding the Southeast Asian Aerosol System by Remote Sensing: An Initial Review and Analysis for the Seven Southeast Asian Studies (7SEAS) Program. Atmos. Res. 122, 403-468, 2013.

Reid., J. S., Xian, P., Hyer, E. J., Flatau, M. K., Ramirez, E. M., Turk, F. J., Sampson, C. R., Zhang, C.,

Fukada, E. M., and Maloney, E. D., Multi-scale meteorological conceptual analysis of observed active fire hotspot activity and smoke optical depth in the Maritime Continent, Atmos. Chem. Phys., 12, 1–31, 2012.

Remer, L. A., Kleidman, R. G., Levy, R. C., Kaufman, Y. J., Tanré, D., Mattoo, S., Martins, J. V., Ichoku, C., Koren, I., Yu, H. and Holben, B. N.: Global aerosol climatology from the MODIS satellite sensors, J. Geophys. Res.-Atmos., 113, D14S07, doi:10.1029/2007JD009661, 2008.

Remer, L. A., Y. J. Kaurman, D. Tanre, S. Mattoo, D. A. Chu, J. V. Martins, R.-R. Li, C. Ichoku, R. C. Levy, R. G. Kleidman, T. F. Eck, E. Vermote, and B. N. Holben: The MODIS aerosol algorithm, products, and validation, J. Atmos. Sci., 62, 947–973, 2005.

Reynolds, R. W., Folland, C. K., and Parker, D. E.: Biases in satellite-derived sea-surface-temperature data, Nature, 341, 728-731, 1989.

Ridley, D. A., C. L. Heald, and J. M. Prospero: What Controls the Recent Changes in African Mineral Dust Aerosol Across the Atlantic? Atmos. Chem. Phys. 14, 5735–5747, 2014.

Ritchie, H.: Semi-Lagranian Advection on a Gaussian Grid, Mon. Wea. Rev., 115, 608-619, 1987.

Robock, A.: Satellite data contamination, Nature, 341, 695-695, 1989.

Saltzman, E.S. , D.B. King, K. Holmen, C. Leck : Experimental determination of the diffusion coefficient of dimethylsulfide in water. J. Geophys. Res., 98, 16481–16486, 1993.

Sapiano, M. R. P. and P. A. Arkin: An intercomparison and validation of high resolution satellite precipitation estimates with three-hourly gauge data. J. Hydromet.,10, 149-166, 2009.

Sekiyama, T. T., T. Y. Tanaka, A. Shimizu, and T. Miyoshi: Data assimilation of CALIPSO aerosol observations, Atmos. Chem. Phys., 10, 39–49, 2010.

Sen, P. K.: "Estimates of the regression coefficient based on Kendall's tau", J. Amer. Stat. Association, 63, 1379–1389, 1968.

Sessions, W. R., Reid, J. S., Benedetti, A., Colarco, P. R., da Silva, A., Lu, S., Sekiyama, T., Tanaka, T. Y., Baldasano, J. M., Basart, S., Brooks, M. E., Eck, T. F., Iredell, M., Hansen, J. A., Jorba, O. C., Juang, H.-M. H., Lynch, P., Morcrette, J.-J., Moorthi, S., Mulcahy, J., Pradhan, Y., Razinger, M., Sampson, C. B., Wang, J., and Westphal, D. L.: Development towards a global operational aerosol consensus: basic climatological characteristics of the International Cooperative for Aerosol Prediction Multi-Model Ensemble (ICAP-MME), Atmos. Chem. Phys., 15, 335-362, 2015.

Shi, Y., J. Zhang, J. S. Reid, B. Liu, and R. Deshmukh: Multi-sensor analysis on data-assimilation-quality MISR aerosol products, Abstract A53C-0358 presented at 2011 Fall Meeting, AGU, San Francisco, Calif., 5-9 Dec, 2011c.

Shi, Y., Zhang, J., Reid, J. S., Holben, B., Hyer, E. J., and Curtis, C.: An analysis of the collection 5 MODIS over-ocean aerosol optical depth product for its implication in aerosol assimilation, Atmos. Chem. Phys., 11, 557–565, 2011a.

Shi, Y., Zhang, J., Reid, J. S., Hyer, E. J., Eck, T. F., Holben, B. N., and Kahn, R. A.: A critical examination of spatial biases between MODIS and MISR aerosol products – application for potential AERONET deployment, Atmos. Meas. Tech., 4, 2823–2836, 2011b.

Shi, Y., Zhang, J., Reid, J. S., Liu, B., and Hyer, E. J.: Critical evaluation of cloud contamination in the MISR aerosol products using MODIS cloud mask products, Atmos. Meas. Tech., 7, 1791-1801, 2014.

Shi, Y., Zhang, J., Reid, J. S., Hyer, E. J., and Hsu, N. C.: Critical evaluation of the MODIS Deep Blue aerosol optical depth product for data assimilation over North Africa, Atmos. Meas. Tech., 6, 949-969, 2013.

Slinn, A. A., and W. G. Slinn: Predictions for particle deposition on natural waters, Atmos. Environ., 14, 1013– 1016, 1980.

Smirnov, A., B. N. Holben, T. F. Eck, O. Dubovik, and I. Slutsker: Cloud screening and quality control algorithms for the AERONET data base, Remote Sens. Environ., 73, 337– 349, 2000.

Song C., Woodcock, C. E., Seto, K. C., Lenny, M. P., Macomber, S. A., Classification and change detection

using Landsat TM data: When and how to correct atmospheric effects? Remote Sens. of Environ., 75, 230-244, 2001.
Staniforth, A. and Côté, J.: Semi-Lagrangian integration schemes for atmospheric models—a review. Mon. Weather Rev., 119, 2206–2223, 1991.
Sun, Y., S. Solomon, A. Dai and R. W. Portmann: How often does it rain? J. Clim., 19, 916-934, 2007.
Tanaka, T. Y., Orito, K., Sekiyama, T. T., Shibata, K., Chiba, M., and Tanaka, H.: MASINGAR, a global tropospheric aerosol chemical transport model coupled with MRI/JMA98 GCM: Model description, Pap. Meteorol. Geophys., 53, 119–138, 2003.
Theil, H.: "A rank-invariant method of linear and polynomial regression analysis. I, II, III", Nederl. Akad. Wetensch., Proc. 53: 386–392, 521–525, 1397–1412. 1950.
Torres, O., Bhartia, P. K., Herman, J. R., Sinyuk, A., Ginoux, P. and Holben, B.: A long-term record of aerosol optical depth from TOMS observations and comparison to AERONET measurements, J. Atmos. Sci., 59, 398–413, 2002.
Tosca, M.G., Randerson, J.T., Zender, C.S., Nelson, D.L., Diner, D.J., Logan, J.A.: Dynamics of fire plumes and smoke clouds associated with peat and deforestation fires in Indonesia. J. Geophys. Res. 116, 2011.
Toth, T.D., J. Zhang, J.R. Campbell, J.S. Reid, Y. Shi, R.S. Johnson, A. Smirnov, M.A. Vaughan, and D.M. Winker: Investigating enhanced Aqua MODIS aerosol optical depth retrievals over the mid-to-high latitude Southern Oceans through intercomparison with co-located CALIOP, MAN, and AERONET data sets, J. Geophys. Res.-Atmos., 118, 4700-4714, 2013.
Uppala, S.M., Kållberg, P.W., Simmons, A.J., Andrae, U., da Costa Bechtold, V., Fiorino, M., Gibson, J.K., Haseler, J., Hernandez, A., Kelly, G.A., Li, X., Onogi, K., Saarinen, S., Sokka, N., Allan, R.P., Andersson, E., Arpe, K., Balmaseda, M.A., Beljaars, A.C.M., van de Berg, L., Bidlot, J., Bormann, N., Caires, S., Chevallier, F., Dethof, A., Dragosavac, M., Fisher, M., Fuentes, M., Hagemann, S., Hólm, E., Hoskins, B.J., Isaksen, L., Janssen, P.A.E.M., Jenne, R., McNally, A.P., Mahfouf, J.-F., Morcrette, J.-J., Rayner, N.A., Saunders, R.W., Simon, P., Sterl, A., Trenberth, K.E., Untch, A., Vasiljevic, D., Viterbo, P., and Woollen, J.: The ERA-40 re-analysis. Quart. J. R. Meteorol. Soc., 131, 2961-3012, 2005.
van der Werf, G.R., et al.: Continental-scale partitioning of fire emissions during the 1997 to 2001 El Nino/La Nina period. Science 303, 73–76. 2004.
Walcek, C. J., R. A. Brost, J. S. Chang and M. L. Wesely: SO2, sulfate and HNO3 deposition velocities computed using regional landuse and meteorological data. Atmos. Environ., 20, 949-964, 1986.
Walker, A. L., M. Liu, S. D. Miller, K. A. Richardson, and D. L. Westphal: Development of a dust source database for mesoscale forecasting in southwest Asia, J. Geophys. Res., 114, D18207, doi:10.1029/2008JD011541, 2009.
Wang, Chunzai, Shenfu Dong, Amato T. Evan, Gregory R. Foltz, Sang-Ki Lee: Multidecadal covariability of north atlantic sea surface temperature, african dust, sahel rainfall, and atlantic hurricanes. J. Climate, 25, 5404–5415. 2012.
Wang, J., Ge, C., Yang, Z., Hyer, E. J., Reid, J. S., Chew, B. N., Mahmud, M., Zhang, Y., Zhang, M., Mesoscale modeling of smoke transport over the Southeast Asian Maritime Continent: Interplay of sea breeze, trade wind, typhoon, and topography, Atmos. Res., 122, 486-503, 2013.
Weatherhead, E. C., Reinsel, G. C., Tiao, G. C., Meng, X.-L., Choi, D., Cheang, W.-K., Keller, T., DeLuisi, J., Wuebbles, D. J., Kerr, J. B., Miller, A. J., Oltmans, S. J., and Frederick, J. E.: Factors affecting the detection of trends: Statistical considerations and applications to environmental data, J. Geophys. Res., 103(D14), 17149–17161, 1998.
Weaver, C., da Silva, A., Chin, M., Ginoux, P., Dubovik, O., Flittner, D., Zia, A., Remer, L., Holben, B., and Gregg, W.: Direct insertion of MODIS radiances in a global aerosol transport model, J. Atmos. Sci., 64, 808–827, 2007.
Westphal, D. L., Curtis, C. A., Liu, M., and Walker, A. L.: Operational aerosol and dust storm forecasting,

in WMO/GEO Expert Meeting on an International Sand and Dust Storm Warning System, IOP Conference Series Earth and Environmental Science, 7, doi: 10.1088/1755-1307/7/1/012007, 2009.
Westphal, D. L., O. B. Toon, and T. N. Carlson: A case study of mobilization and transport of Saharan dust. J. Atmos. Sci., 45, 2145-2175, 1988.
Wiedinmyer, C., S.K. Akagi, R.J. Yokelson, L.K. Emmons, J.A. Al-Saadi, J.J. Orlando, and A.J. Soja: The Fire INventory from NCAR (FINN): A high resolution global model to estimate the emissions from open burning. Geoscientific Model Development, 4, 625-641, 2011.
Wilcox E. M. and V. Ramanathan: The impact of observed precipitation upon the transport of aerosols from South Asia, Tellus-B, 56, 435-450, 2004.
Wilkinson, S. M., Dunn, S., Ma, S.: The vulnerability of the European air traffic network to spatial hazards, Natural hazards, 60, 1027-1036, 2012
Witek, M. L., P. J. Flatau, P. K. Quinn, and D. L. Westphal: Global sea-salt modeling: Results and validation against multicampaign shipboard measurements, J. Geophys. Res., 112, 2007.
Xian, P., J. S. Reid, J. F. Turk, E. J. Hyer and D. L. Westphal: Impact of models versus satellite measured tropical precipitation on regional smoke optical thickness in an aerosol transport model, Geophys. Res. Lett., 36, L16805, doi:10.1029/2009GL038823, 2009.
Xian, P., J. S. Reid, S. A. Atwood, R. S. Johnson, E. J. Hyer, D. L. Westphal, W. Sessions: Smoke aerosol transport patterns over the Maritime Continent. Atmos. Res., 122, 469-485, 2013.
Young, I. R., S. Zieger, and A. V. Babanin: Global trends in wind speed and wave height, Science, 332, 451–455, 2011.
Zhang, J. and Reid, J. S.: A decadal regional and global trend analysis of the aerosol optical depth using a data-assimilation grade over-water MODIS and Level 2 MISR aerosol products, Atmos. Chem. Phys., 10, 10949–10963, 2010.
Zhang, J. and Reid, J. S.: An analysis of clear sky and contextual biases using an operational over ocean MODIS aerosol product, Geophys. Res. Lett., 36, L15824, doi:10.1029/2009GL038723, 2009.
Zhang, J. and Reid, J. S.: MODIS Aerosol Product Analysis for Data Assimilation: Assessment of Level 2 Aerosol Optical Thickness Retrievals, J. Geophys. Res.-Atmos., 111, 22207, doi:10.1029/2005JD006898, 2006.
Zhang, J., J. R. Campbell, E. J. Hyer, J. S. Reid, D. L. Westphal, and R. S. Johnson: Evaluating the impact of multisensory data assimilation on a global aerosol particle transport model, J. Geophys. Res. Atmos., 119, 4674–4689, 2014.
Zhang, J., J. R. Campbell, J. S. Reid, D. L. Westphal, N. L. Baker, W. F. Campbell, and E. J. Hyer: Evaluating the impact of assimilating CALIOP-derived aerosol extinction profiles on a global mass transport model, Geophys. Res. Lett., 38, L14801, doi:10.1029/2011GL047737, 2011.
Zhang, J., Reid, J. S., Westphal, D. L., Baker, N. L., and Hyer, E. J.: A system for operational aerosol optical depth data assimilation over global oceans, J. Geophys. Res., 113, D10208, doi:10.1029/2007JD009065, 2008.
Zhang, Q., et al: Ubiquity and dominance of oxygenated species in organic aerosols in anthropogenically-influenced Northern Hemisphere midlatitudes, Geophys. Res. Lett., 34, L13801, doi:10.1029/2007GL029979. 2007.

1158

1159

1160 Table 1. Optical properties for dry aerosol particles at 550 nm in NAAPS.

Species	a_{eff}(μm)	α_{ext} (m^2 g^{-1})	α_{scat} (m^2 g^{-1})	α_{abs} (m^2 g^{-1})	$\omega_\circ$	g
ABF	0.14	3.48	3.13	0.35	0.90	0.60
Dust	2.50	0.59	0.52	0.07	0.88	0.73
Smoke	0.17	4.48	3.99	0.50	0.89	0.58
Sea Salt	1.50	1.42	1.41	0.01	0.99	0.68

1161 where α_{ext}, α_{scat}, *and* α_{abs} are the bulk mass extinction, scattering, and absorption efficiencies, $\omega_\circ$ the
1162 single scattering albedo and *g* the asymmetry factor. a_{eff} is the bulk effective radius. "ABF" stands for
1163 anthropogenic and biogenic fine particles.

1164

Table 2. List of AERONET sites for further validation and statistics of the reanlaysis total AOT at 550 nm compared with AERONET at these sites for December 2011-November 2012 breaking into two seasons DJFMAM (winter) and JJASON (summer). The selected sites and time periods match Sessions et al. (2015), where the International Cooperative for Aerosol Prediction (ICAP) Multi Model Ensemble (ICAP-MME) AOT is described and evaluated. The mean of total AOT of AERONET L2 data, the paired reanalaysis data bias, root mean square error (RMSE), square of the Pearson correlation coefficient (r^2) and the total number of AERONET 6-hourly data (N) are shown. Values in bold, bold with underline and italic mean that the reanalysis is equally good, better and worse than the ICAP MME mean respectively (Such comparison is not available in terms of r^2 or for the fine mode AOT).

Note: Correlation is not calculated for sites with dynamical range of the AOT data less than 0.1; correlation is marked with "N/A*" for these sites. "N/A" means data is not available.

Seasonal AOT means for sites with only a few AERONET data (N) may not be representative.

Site	Location	Main Aerosol type	Mean AERONET total 550 nm AOT winter|summer		Bias winter | summer		RMSE winter | summer		r^2 winter | summer		N winter | summer	
Alta Floresta	Brazil, 9S, 56W	Smoke	0.12	0.29	**0.00**	*-0.03*	**0.05**	**0.11**	0.49	0.82	35	203
Baengnyeong	Yellow Sea, 37N, 124E	ABF, Dust	0.39	0.34	**0.04**	**0.00**	**0.16**	**0.18**	0.77	0.75	213	215
Banizoumbou	Sahel, 13N, 2E	Dust	0.67	0.42	*-0.11*	**-0.08**	*0.35*	**0.21**	0.53	0.51	493	396
Beijing	China, 39N, 116E	ABF, Dust	0.60	0.62	*-0.14*	*-0.17*	*0.50*	**0.45**	0.54	0.76	322	110
Capo Verde	Sub-tro. Atlantic, 16N, 22W	Dust	0.36	0.39	**0.02**	**0.00**	**0.12**	*0.12*	0.88	0.77	283	312
Cart Site	Great Plains, 36N, 97W	Clean	0.10	0.14	**0.00**	**-0.01**	*0.05*	**0.05**	0.65	0.63	335	419
Chapais	Quebec, 49N, 74W	Clean	N/A	0.12	N/A	**0.00**	N/A	**0.05**	N/A	0.72	0	112
Chiang Mai	Thailand, 18N, 98E	Smoke	0.63	0.23	**-0.14**	*-0.05*	**0.27**	*0.11*	0.82	0.44	297	161
Crozet Island	Southern Ocean, 46S, 51E	Sea Salt	0.04	0.05	*0.03*	**0.03**	**0.05**	**0.05**	N/A*	N/A*	18	41
Gandhi College	Rural India, 25N, 84E	Dust, ABF	0.60	0.70	**-0.08**	**-0.08**	**0.15**	**0.30**	0.71	0.35	315	311
GSFC	EAST CONUS, 38N, 76W	ABF	0.11	0.18	**0.00**	**-0.01**	**0.05**	**0.07**	0.63	0.71	272	297
Ilorin	Sahel, 8N, 4E	Smoke, Dust	0.99	0.30	**-0.09**	**0.02**	**0.31**	*0.13*	0.75	0.55	411	182
Kanpur	Urban India, 26N, 80E	ABF, Dust	0.61	0.70	**-0.08**	**-0.02**	**0.19**	**0.27**	0.61	0.21	385	281
Minsk	Western Asia, 53N, 27E	ABF, Smoke	0.14	0.15	**0.00**	**-0.01**	*0.06*	**0.07**	0.52	0.51	156	180
Moldova	Eastern Europe, 47N, 28E	ABF	0.19	0.17	**0.00**	**0.00**	**0.07**	**0.07**	0.42	0.59	197	347
Monterey	WEST CONUS, 36N, 121W	Clean	0.08	0.07	**0.02**	**-0.01**	**0.04**	**0.03**	0.53	0.31	80	77
Palma de Mallorca	Mediterranean, 39N, 2E	Dust, ABF	0.08	0.20	**0.00**	*-0.02*	**0.02**	**0.06**	0.85	0.85	24	401
Ragged Point	Caribbean, 13N, 59W	African Dust	0.15	0.21	**0.00**	**0.01**	**0.05**	*0.06*	0.81	0.87	285	227
Rio Branco	Brazil, 9S, 67W	Smoke	0.08	0.22	**0.00**	**-0.02**	*0.04*	**0.08**	N/A*	0.86	144	328
Singapore	Maritime Cont., 1N, 103E	ABF, Smoke	0.31	0.47	*-0.12*	*-0.16*	*0.20*	*0.24*	0.15	0.55	71	192
Solar Village	Southwest Asia, 24N, 46E	Dust	0.63	0.38	**0.02**	*0.07*	*0.27*	*0.13*	0.25	0.68	77	318

1177

1178

1179

1180 Table 3. Same as Table 2, except for fine-mode AOT at 550 nm.

Site	Mean AERONET fine AOT winter|summer		Bias winter | summer		RMSE winter | summer		r^2 winter | summer		N winter | summer	
Alta Floresta	0.07	0.21	0.02	0.02	0.04	0.11	0.49	0.77	35	203
Baengnyeong	0.26	0.25	0.04	0.01	0.14	0.16	0.75	0.74	213	215
Banizoumbou	0.15	0.07	-0.03	0.07	0.14	0.11	0.17	0.16	493	396
Beijing	0.37	0.47	-0.05	-0.10	0.32	0.34	0.57	0.79	322	110
Capo Verde	0.08	0.06	0.01	0.03	0.07	0.05	0.33	0.30	283	312
Cart Site	0.06	0.09	0.01	0.02	0.03	0.04	0.69	0.70	335	419
Chapais	N/A	0.08	N/A	0.02	N/A	0.05	0.00	0.73	0	112
Chiang Mai	0.50	0.14	-0.04	0.02	0.22	0.08	0.82	0.48	297	161
Crozet Island	0.01	0.02	-0.01	-0.01	0.01	0.01	N/A*	N/A*	18	41
Gandhi College	0.31	0.43	0.02	0.05	0.11	0.23	0.71	0.41	315	311
GSFC	0.07	0.13	0.01	0.01	0.04	0.06	0.59	0.72	272	297
Ilorin	0.36	0.13	0.00	0.08	0.15	0.13	0.50	0.23	411	182
Kanpur	0.34	0.41	0.01	0.06	0.14	0.26	0.71	0.27	385	281
Minsk	0.09	0.10	0.01	0.01	0.04	0.05	0.53	0.47	156	180
Moldova	0.11	0.11	0.02	0.02	0.06	0.06	0.44	0.59	197	347
Monterey	0.03	0.04	0.02	0.00	0.02	0.02	N/A*	N/A*	80	77
Palma de Mallorca	0.05	0.09	0.00	0.00	0.02	0.03	0.91	0.61	24	401
Ragged Point	0.03	0.03	0.02	0.01	0.03	0.02	N/A*	N/A*	285	227
Rio Branco	0.04	0.16	0.01	0.03	0.02	0.08	N/A*	0.86	144	328
Singapore	0.21	0.34	-0.04	-0.07	0.14	0.18	0.13	0.58	71	192
Solar Village	0.11	0.13	0.07	0.06	0.09	0.07	0.09	0.36	77	318

1181

1182

1183

1184 Table 4, same as Table 2, except for coarse-mode AOT at 550 nm and for sites in which the coarse mode
1185 is dominated by dust.

1186

Site	Mean AERONET coarse AOT		Bias		RMSE		r^2		N	
	winter	summer	winter	summer	winter	summer	winter	summer	winter	summer
Baengnyeong	0.13	0.09	**0.00**	**-0.01**	*0.07*	**0.05**	0.47	0.63	213	215
Banizoumbou	0.52	0.35	*-0.08*	*-0.15*	*0.29*	*0.23*	0.50	0.55	493	396
Beijing	0.24	0.15	*-0.09*	*-0.07*	*0.31*	*0.16*	0.12	0.37	322	110
Capo Verde	0.28	0.33	**0.01**	*-0.04*	**0.09**	*0.12*	0.89	0.74	283	312
Gandhi College	0.29	0.27	*-0.10*	*-0.13*	*0.14*	*0.23*	0.50	0.57	315	311
Ilorin	0.63	0.17	*-0.09*	*-0.06*	*0.30*	*0.11*	0.65	0.49	411	182
Kanpur	0.27	0.29	*-0.09*	**-0.09**	*0.14*	*0.15*	0.65	0.69	385	281
Palma de Mallorca	0.03	0.11	**0.00**	*-0.02*	**0.01**	*0.05*	0.53	0.83	24	401
Ragged Point	0.12	0.18	**-0.02**	**-0.01**	**0.06**	**0.06**	0.72	0.85	285	227
Solar Village	0.52	0.25	*-0.05*	**0.01**	*0.24*	*0.10*	0.24	0.71	77	318

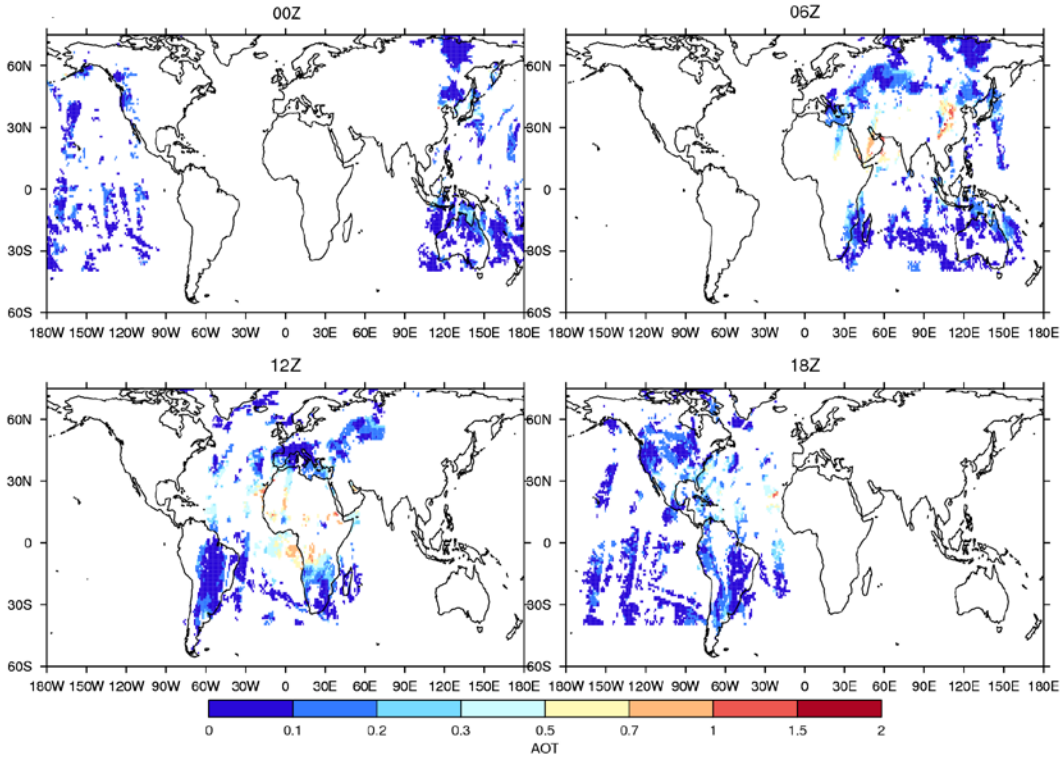

Figure 1. An example of the general pattern of data coverage from MODIS (Aqua + Terra) and MISR for each AOT assimilation cycle at the valid time of the analysis, ie., 0, 6 , 12 and 18 UTC, in NAVDAS-AOT. The MODIS and MISR AOT data displayed here is after strict QA/QC processes for Aug 11, 2011. The MODIS and MISR data assimilated in each NAVDAS-AOT cycle were acquired in a 6-hour range centered on the nominal valid time of the analysis.

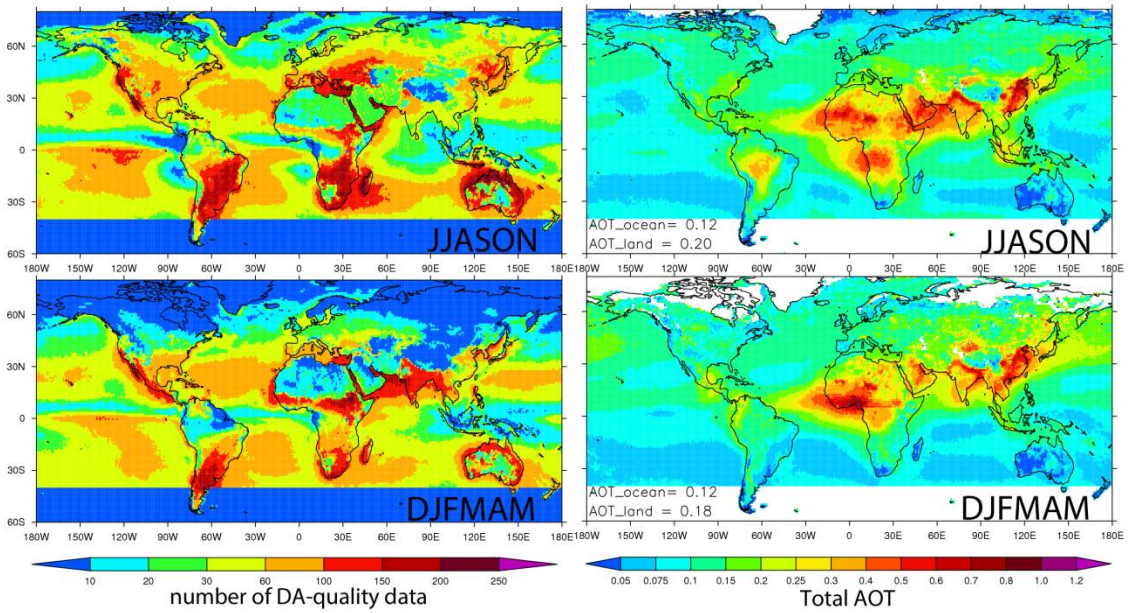

Figure 2. Properties of the 6-hourly 1x1 degree MODIS+MISR data assimilation quality AOT data for JJASON (June-November, upper) and DJFMAM (Previous year December-May, lower) averaged over 2003-2013 (June 2003-May 2013): Left) total number of the DA-quality data, Right) seasonal mean of the total AOT at 550 nm. Blank area indicates no available data. Annotations at the bottom left in the AOT figures show the area mean AOTs over ocean and over land averaged for 40°S-60°N.

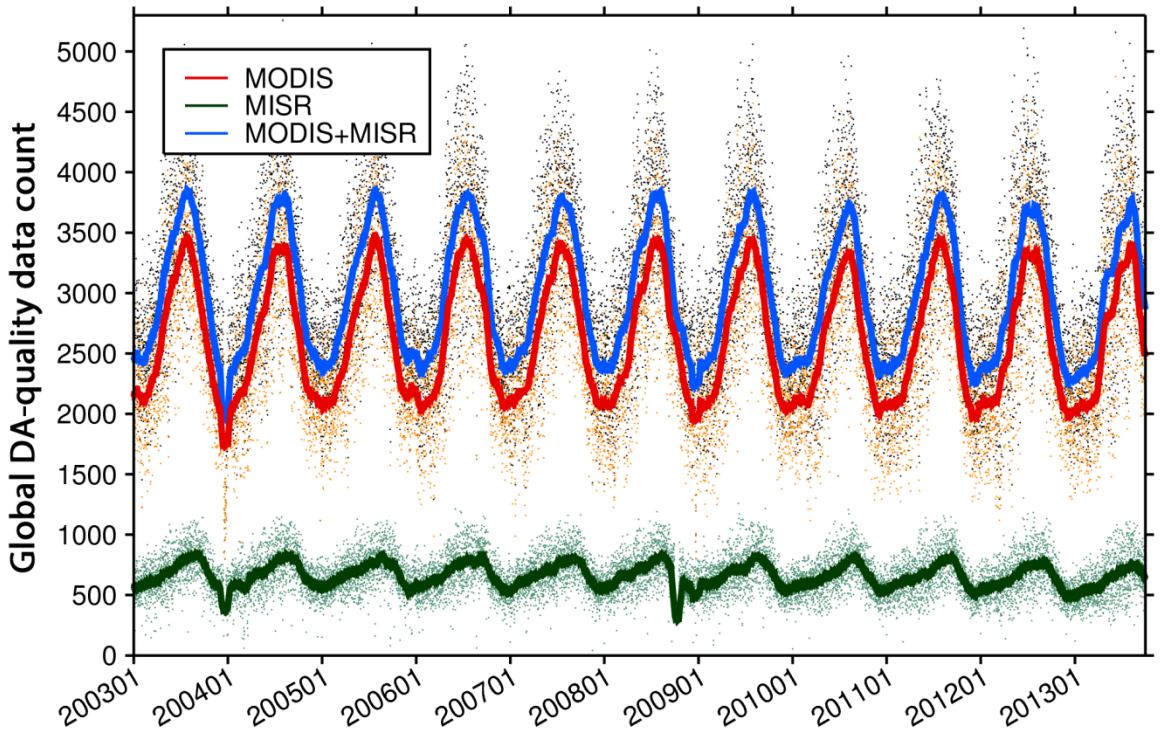

Figure 3. The time series of 6-hourly data count of the global 1x1 grid MODIS (Terra+Aqua) (red), MISR (green), and fused MODIS-MISR data assimilation quality AOT (blue). Dots show 6-hourly data counts, and the solid lines represent the 30-day running average. The seasonal variation of the data volume is mainly related to the fact that more AOT data are discarded for the southern hemisphere high latitudes than the northern hemisphere high latitudes considering cloud contamination (see text for details).

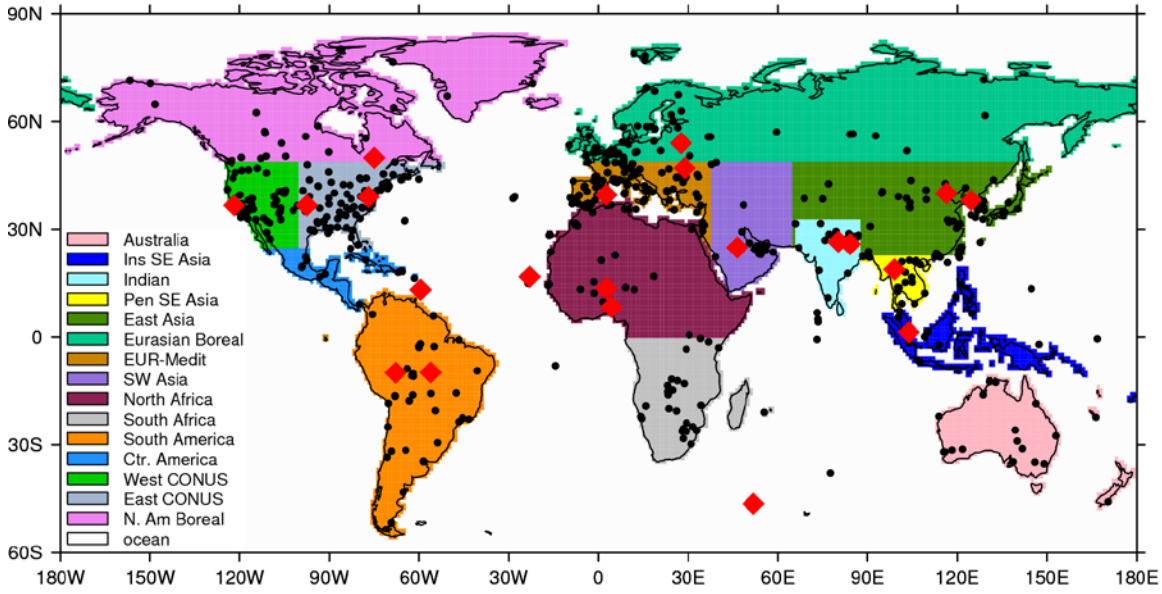

1211

1212 Figure 4. Selection of regions for this study. Antarctica is excluded. All AERONET sites that have valid L2
1213 data for the study period (2003-2013) are in black dots. The selected sites for detailed validation
1214 (Section 3.2.3) are highlighted with red diamonds.

1215

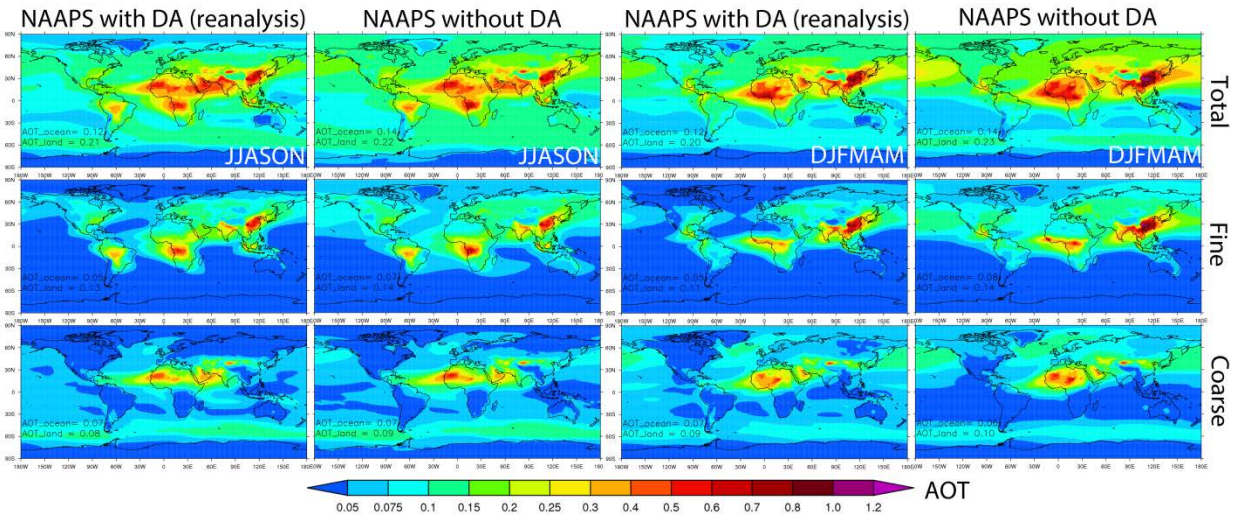

1216

1217 Figure 5. 2003-2013 averaged biseasonal (June-November, ie., JJASON, and December-May, ie.,
1218 DJFMAM) total (upper), fine (middle) and coarse (bottom) AOTs at 550 nm from NAAPS with and
1219 without AOT data assimilation. Annotations at the bottom left in the figures show the area mean AOTs
1220 over ocean and over land averaged for 40°S-60°N.

1221

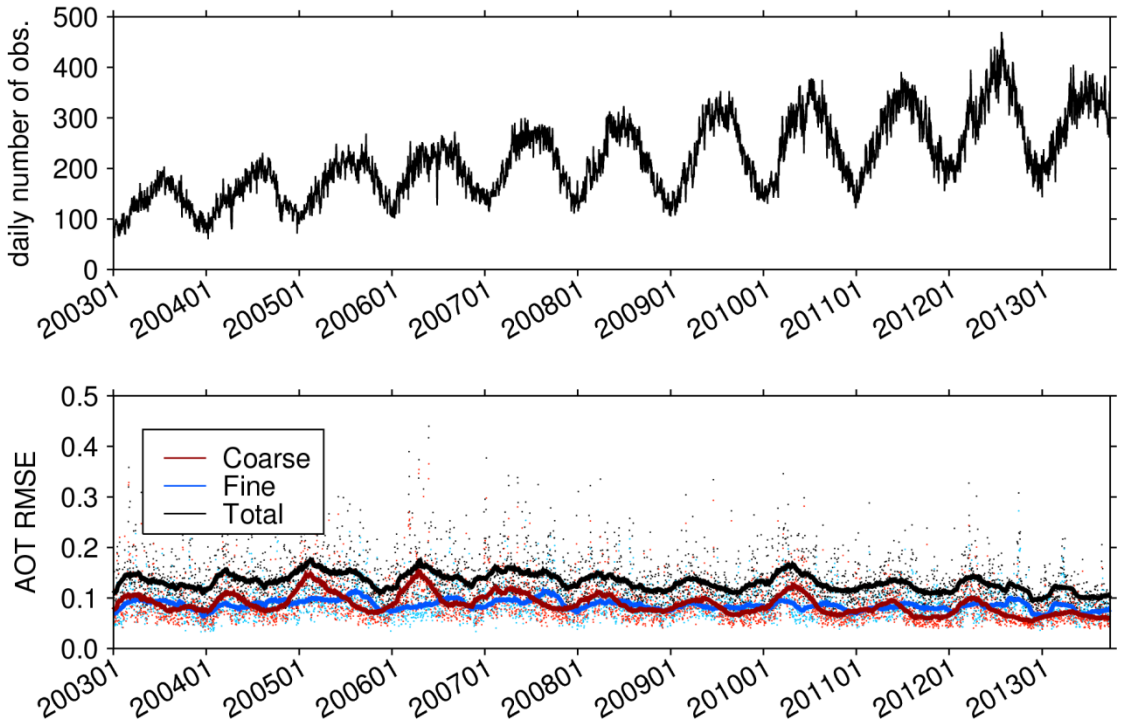

Figure 6. a) Time series of the daily total number of global regular AERONET L2 observations (excluding observations at DRAGON sites) binned into 6-hourly intervals (to match the model output resolution) for the AOT reanalysis period. b) Time series of the RMSE of the reanalysis total AOT (black), fine-mode AOT (blue) and coarse-mode AOT (red), all at 550 nm, validated with AERONET. The daily average 6-hr RMSEs are in small dots and the corresponding 90-day running averages are in solid lines.

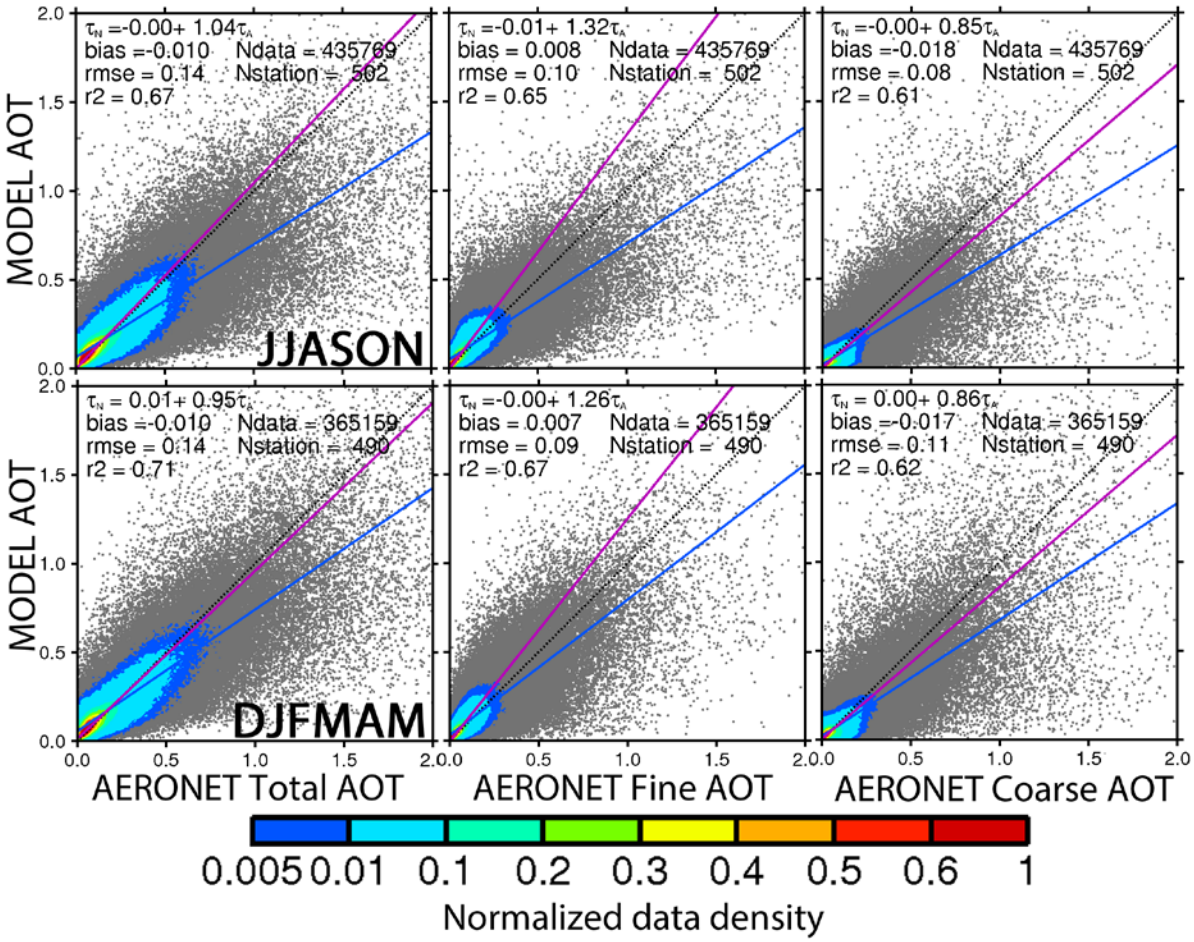

Figure 7. Pair-wise comparison of the global 6-hourly reanalysis AOT and AERONET AOT with respect to total (left), fine (middle) and coarse (right) modes at 550 nm for JJASON (upper) and DJFMAM (bottom) for the entire reanalysis time (2003-2013). The normalized data density is shown in color. The solid magenta line represents a Theil-Sen linear regression and the corresponding equation is shown, where τ_N is the NAAPS reanalysis AOT and τ_A is the AERONET AOT. The solid blue line is a least-squares linear regression and the corresponding equation is not shown. Also shown are the bias, root mean square error (rmse), square of the pearson's correlation coefficient (r^2), total number of stations (Nstation) and total number of 6-hourly AERONET data (Ndata).

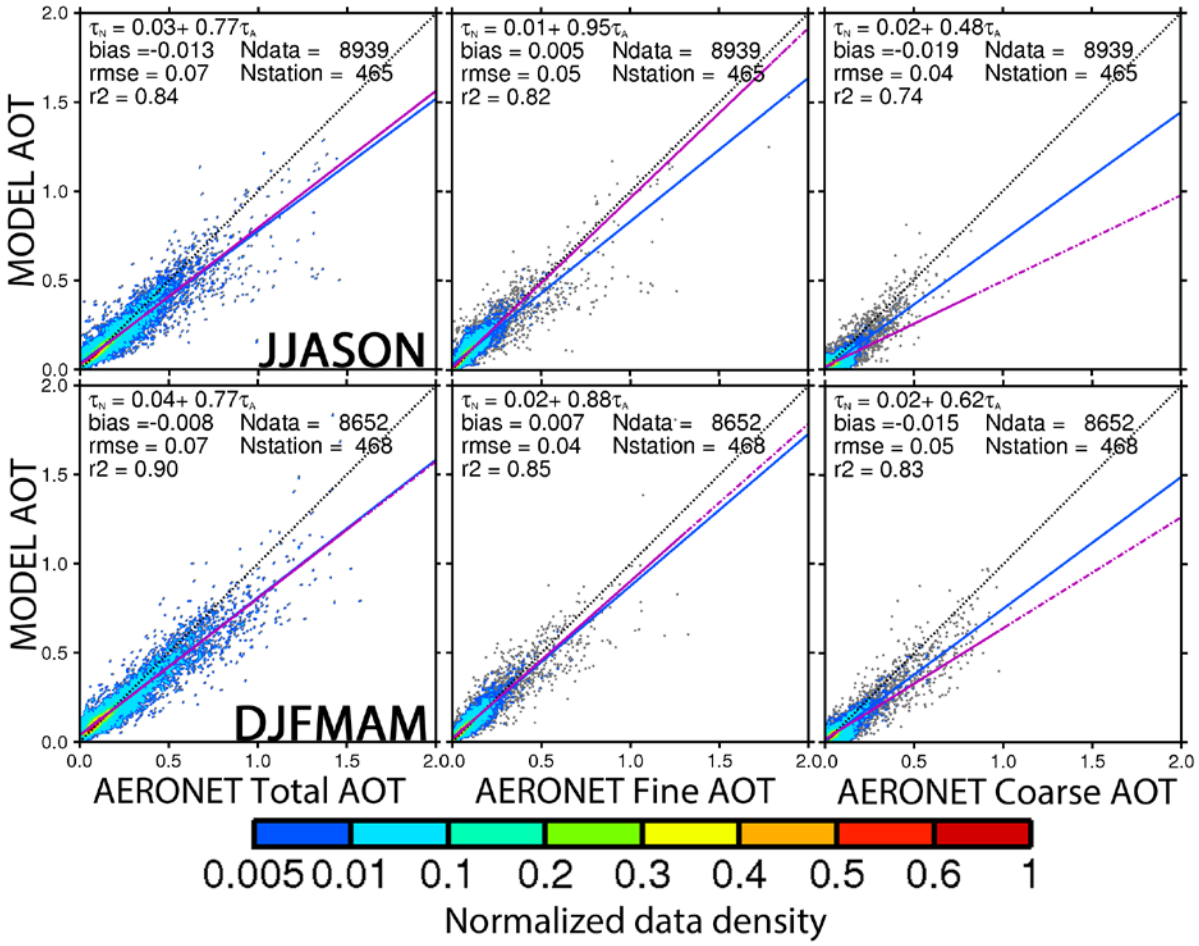

Figure 8. Same as Fig. 7, except for the monthly average of pair-wised 6-hourly mode AOTs at 550 nm. Monthly average is obtained only when the total number of 6-hourly AERONET data exceeds 10 to ensure temporal representativeness. The monthly average reanalysis AOT here is calculated based on the available 6-hourly data that can be paired with AERONET data.

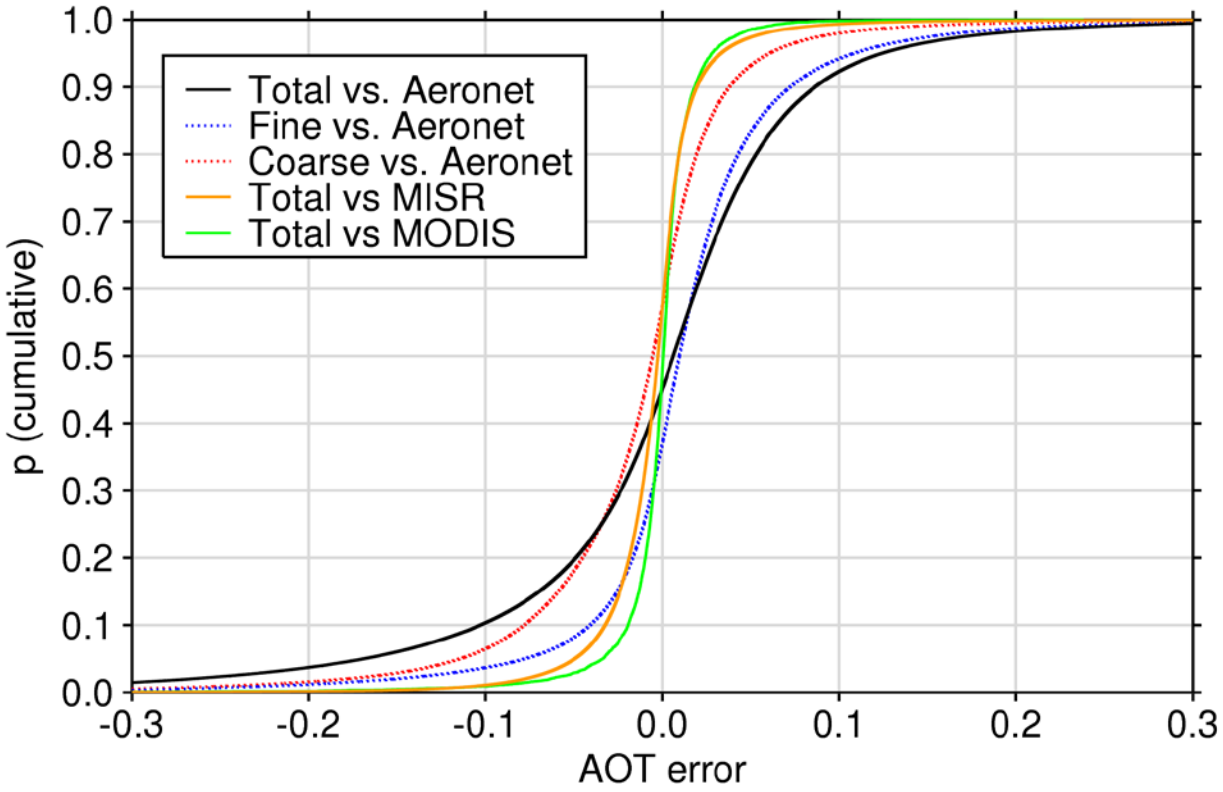

Figure 9. Cumulative distribution function for the reanalysis 6-hourly AOT errors compared to AERONET L2, MODIS and MISR data assimilation quality data with respect to the available total, fine and coarse modes at 550 nm for the entire reanalysis time period (2003-2013).

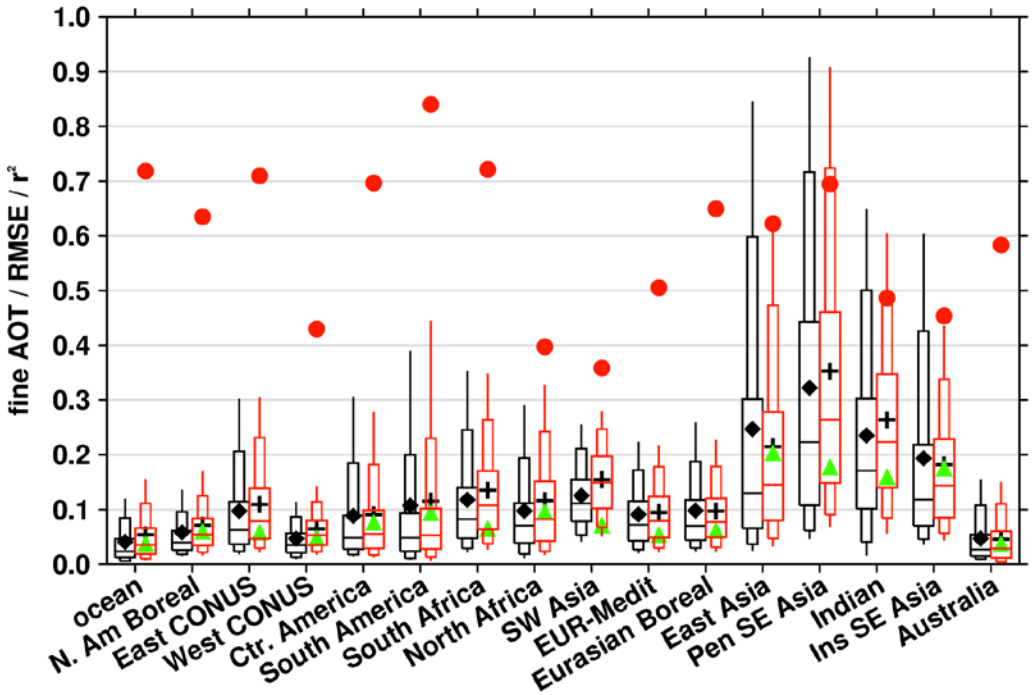

Figure 10. Comparison of regional fine mode AOT at 550 nm of the reanalysis (red) at 95%, 90%, 75%, 50%, 25%, 10% and 5% percentiles to the pair-wised AERONET L2 data (black) for the regions defined in Figure 4 for the 10 year time period (June 2003-May 2013). Also shown are the regional mean of the reanalysis and AERONET fine mode AOTs in "+" and diamond respectively. Green triangles represent the root mean square error (RMSE) of the reanalysis. Red dots represent the square of the Pearson correlation coefficient (r^2) between the reanalysis and the AERONET observations.

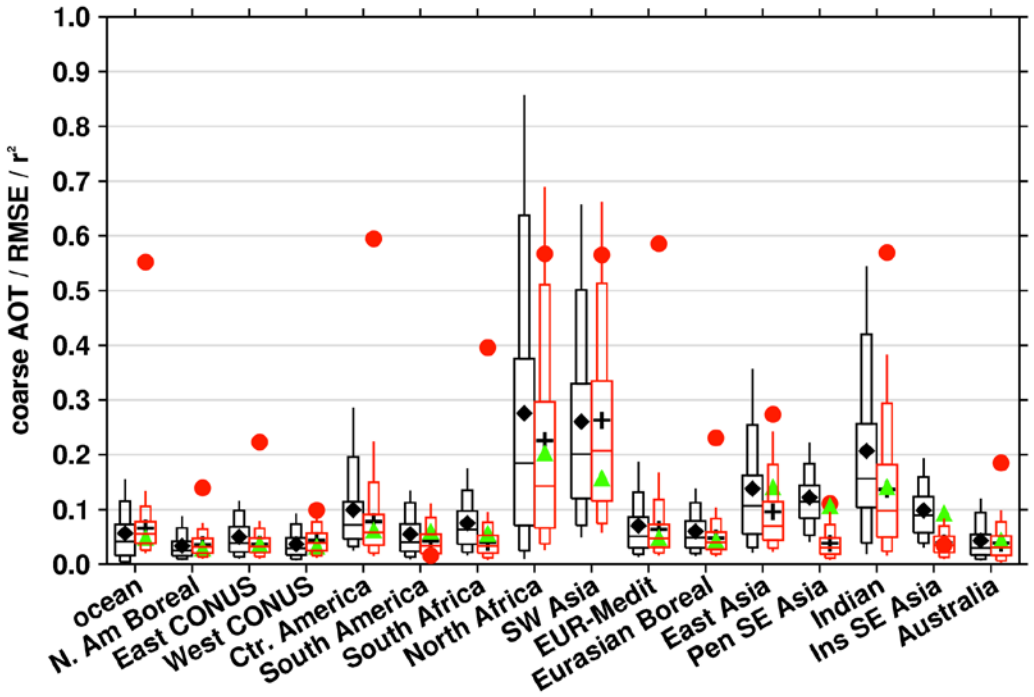

1262

1263 Figure 11. Same as Fig. 10, except for coarse mode AOT at 550 nm.

1264

1265

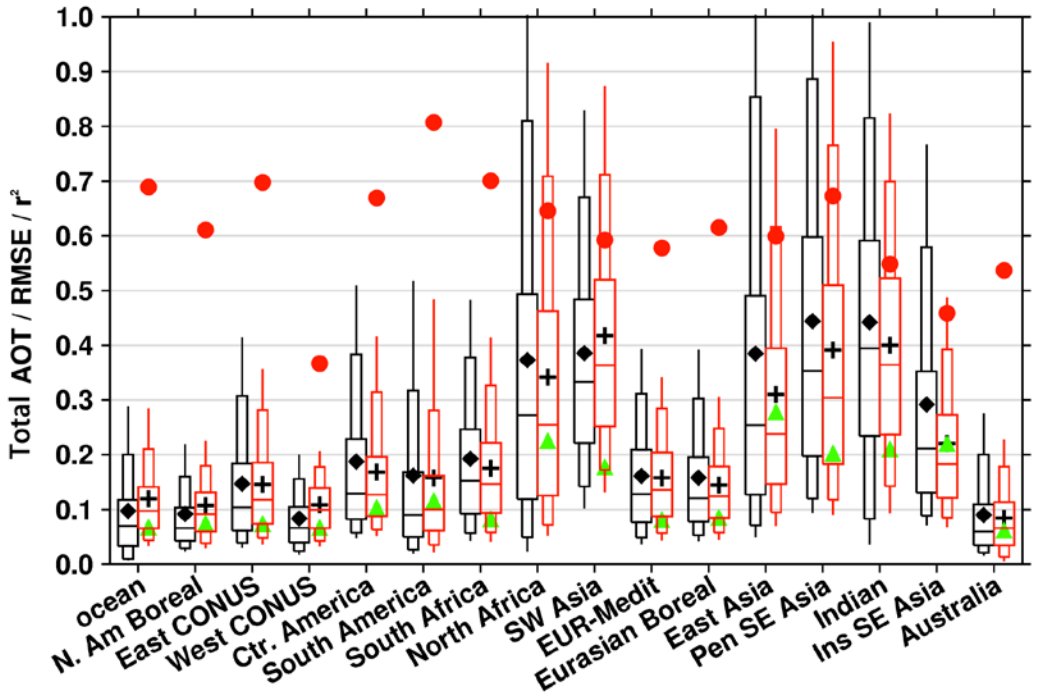

1266

1267 Figure 12. Same as Fig. 10, except for total AOT at 550 nm. Also, AOT value greater than 1.0 is cropped in
1268 this figure.

1269

1270

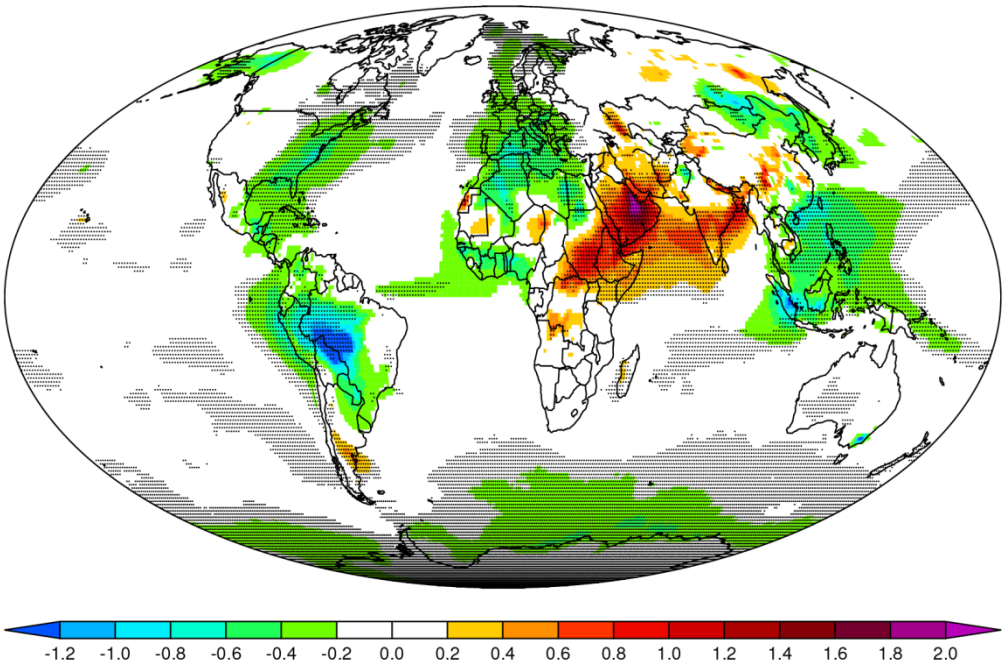

1271

1272 Figure 13. Trends of the deseasonalized reanalysis total AOT at 550 nm over 2003-2013 (unit:
1273 100xAOT/year). The dotted areas have passed 95% statistical significance level (see text and Zhang and
1274 Reid (2010) for details).

1275

1276

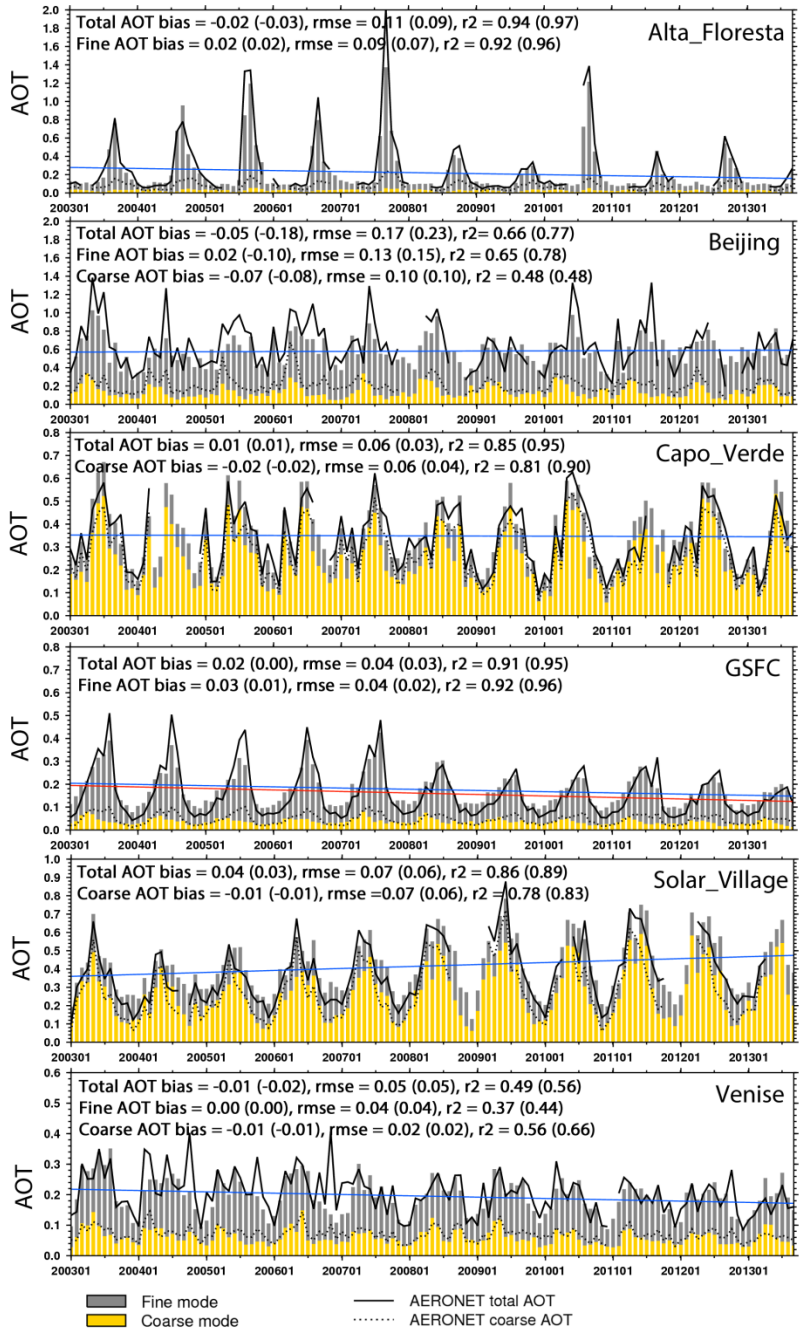

Figure 14. Monthly mean 550 nm reanalysis and AERONET L2 mode AOTs at 6 AERONET sites, Alta Floresta in the Amazon, Beijing in East Asia, Capo Verde off the west coast of North Africa, GSFC in East CONUS, Solar Village in Arabian Peninsula, and Venise in Italy. The solid blue line is a linear regression of the reanalysis total AOT. The red solid line is a linear regression of the AERONET total AOT, only available when there is continuous data through the time. Monthly mean AERONET AOT is obtained only when the total number of 6-hourly AERONET data exceeds 10 to ensure temporal representativeness. Annotations for each time series show bias, RMSE and r^2 of monthly averages for unpaired comparisons; paired comparisons, using reanalysis values sampled to match available AERONET data, are shown in parentheses.

APPENDIX: Impact of tuning of sources and sinks vs. AOT data assimilation upon model performance

To show the relative importance of the tuning process on sources and sinks versus the AOT data assimilation to reanalysis performance, four model runs with difference configurations were conducted. AOT results from these four runs were inter-compared and validated with AERONET L2 data. The four model configurations are NAAPS without tuning (that is to say the original native version of NAAPS from which the reanalysis was originally based), NAAPS with tuning, NAAPS without tuning but with AOT data assimilation, and the final reanalysis version, which is with both tuning and AOT assimilation. The four model runs all cover Dec 2010-Nov 2011 one year time period. Interannual tuning was not conducted to preserve a measure of consistency within the model itself. The AOT data assimilation process, the input data and its pre-DA treatment are kept the same for the DA runs. The "tuning" processes on the sources and sinks include the addition of organic aerosols, updated SO_2 and DMS emissions, use of CMORPH precipitation to replace model precipitation within 30°S-30°N, usage of the FLAMBE MODIS 2-day-maximum regionally tuned smoke emissions and applying regional tuned factors on dust erodible fraction. For example, through the tuning exercises dust emission for 2011 is reduced from 1510 Tg to 953 Tg, and biomass turning smoke emission is reduced from 180 Tg to 85 Tg globally.

The appendix table shows the 550 nm total, fine and coarse mode AOT bias, RMSE, r^2 and Theil-Sen linear regression slope against AERONET from the four model runs. With the tuning of sources and sinks, RMSE decreases about half, bias and r^2 also significantly improved for coarse, fine and total AOTs for the natural model run. The linear regression slope is also much closer to 1 for the fine and the total AOTs, and about unchanged for the coarse AOT compared to the NAAPS run without sources and sinks tuning. The absolute bias, RMSE and r^2 are comparable with those of the DA run without the tuning; i.e., through the tuning process on the baseline ("NAAPS_untuned"), similar validation result can be obtained as through the AOT assimilation on the baseline. This indicates that the tuning process on sources and sinks is as equally important as the AOT data assimilation process.

AOT data assimilation based on the tuned NAAPS further improves the validation statistics. For example, the RMSE is reduced about 20% for the coarse, fine and total AOTs comparing the reanalysis to the "NAAPS_tuned". When comparing the DA runs ("reanalysis" vs. "DA_untuned"), there are also discernable improvements on bias, RMSE and r^2 resulted from the tuning process. The linear regression slope is improved for the fine AOT and about the same for the total AOT. The regression slope is worsened for the coarse AOT (0.64 for the reanalysis), because the model, like other aerosol models, faces challenges successfully resolving dust events over Sahel, East Asia and Indian subcontinent regions (e.g., Sessions et. al. 2015). While the untuned model has slight high biased coarse AOT, which makes the regression slope more tilted. The linear regression slope of the reanalysis based on all the 11-year data is 0.85 (Fig.7) though, better than the 2011 level.

The appendix Fig. 1 and Fig. 2 show the global coarse, fine and total AOT distributions from the four model runs for the two seasons of 2011, ie., JJASON and DJFMAM respectively. For both seasons, it is obvious that the natural NAAPS run without tunings has the most different AOT distributions and global averages among the four runs. The three other runs look more similar to each other, which is consistent with the validation statistics shown in appendix Table 1. For JJASON the natural NAAPS run without tunings has the lowest global mean AOTs among the four runs, yet the highest AOTs near dust and smoke source regions in South America and South Africa. This indicates possible excessive emissions in these regions and excessive removals over water, which are tuned through applying smaller emission factors for smoke and dust and lower dry deposition velocity for dust over water in the tuning process. For both seasons, the tuned NAAPS run without DA has slight high bias in the fine AOT (see also appendix Table 1) and the bias is slightly larger in DJFMAM than in JJASON, most probably resulted from excessive addition of organic aerosols during boreal winter.

Compared to the reanalysis, the DA run without source and sink tuning, exhibits similar global total AOT distribution. However, some differences between the two are noticeable for the fine and coarse AOTs. For example, over the Indian subcontinent the AOT partitioning between the fine and coarse AOTs differs significantly. The contribution of the fine-mode aerosols to the total AOT dominates the contribution of the coarse-mode aerosols in the reanalysis. Whereas the total AOT is predominantly attributed to the coarse-mode aerosols in the DA run without tunings. Over the southern flank of the Himalayas, where fine-mode aerosols from industrial and biofuel emissions often prevails over coarse-mode (refer to Kanpur site in Tables 2-4), the fine mode fraction is increased from ~0.3 in the DA run without tunings to ~0.7 in the reanalysis. This illustrates the importance of the tuning processes in yielding a better AOT partitioning between the fine and coarse modes.

Appendix Table: Statistics of the coarse, fine and total AOTs at 550 nm from four model runs compared with AERONET L2 data. The four model runs are from four different model configurations, including NAAPS without sources and sinks tuning, NAAPS with tuning, NAAPS without tuning but with AOT data assimilation, and the reanalysis version, which is with both the tuning and the AOT assimilation. The comparison is based on one year time period (Dec. 2010 to Nov. 2011). The global AERONET mean is 0.085, 0.102 and 0.187 for coarse, fine and total AOT respectively, obtained with averaging 97654 valid 6-hourly L2 data from 285 stations.

	AOT Bias Coarse | fine | total	RMSE Coarse | fine |total	r^2 Coarse |fine |total	Regression slope Coarse |fine |total
NAAPS_untuned	0.008|-0.030|-0.022	0.17|0.19|0.26	0.33|0.05|0.15	0.59|0.69|0.81
NAAPS_tuned	-0.005|0.021|0.016	0.10|0.10|0.16	0.45|0.47|0.48	0.58|0.98|0.89
DA_untuned	0.014|-0.025|-0.011	0.09|0.11|0.14	0.58|0.41|0.56	0.90|0.75|0.80
Reanalysis	-0.013|0.006|-0.007	0.08|0.08|0.13	0.59|0.63|0.65	0.64|1.00|0.77

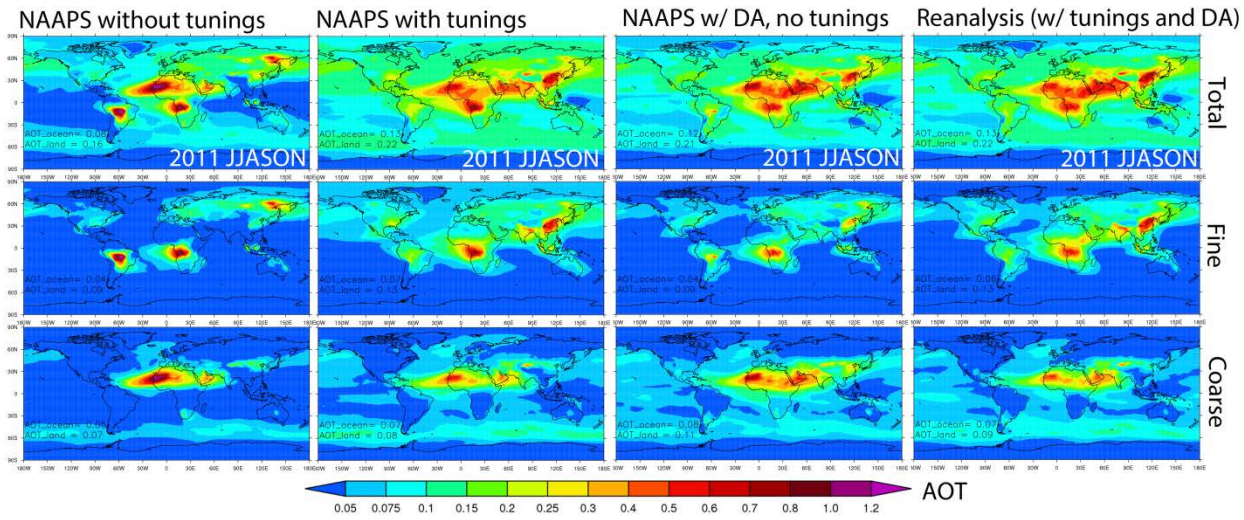

Appendix Figure 1. 6-month-average (Jun-Nov 2011) total (upper), fine (middle) and coarse (bottom) AOTs at 550 nm from four NAAPS runs with different configuration: NAAPS without tuning, NAAPS with tuning processes on sources and sinks, NAAPS without tuning but with AOT data assimilation, and the reanalysis version, which is with both tuning and AOT assimilation. Annotations at the bottom left in the figures show the area mean AOTs over ocean and over land averaged for 40°S-60°N.

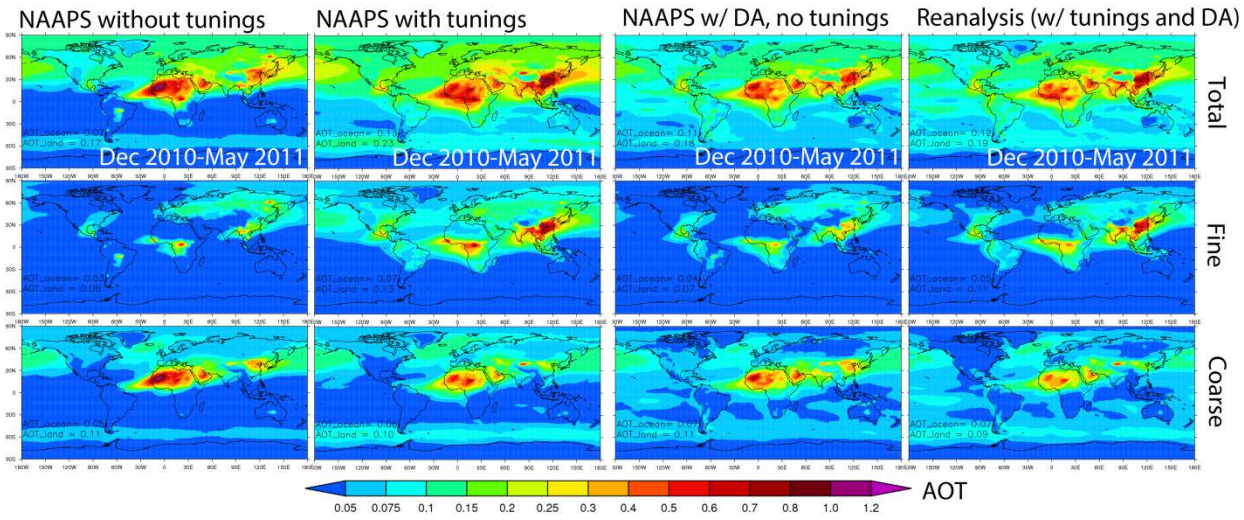

Appendix Figure 2. Same as the Appendix Figure 1, except for Dec. 2010-May 2011 6-month-average.